

## Chapter 5

# Silicon PIN Detectors in Astronomy

### 5.1 Observations with the Kitt Peak 2.1m Telescope

We observed on the 2.1m telescope at the KPNO observatory in Tucson, Arizona ( $110^{\circ} 58' 0''$  W,  $32^{\circ} 13' 0''$  N) during three separate runs in 4/07, 11/07, and 12/07. On each run, a different detector was tested: H4RG-10-007 on the first, H1RG-022 on the second, and H2RG-32-147 on the third. A picture of the RIDL dewar and electronics mounted to the telescope is shown in Figure 5.1. The dewar was placed at the Cassegrain focus, with the telescope delivering an f7.6 beam to the focal plane. Since the pixel size and dimensions of each detector were slightly different, the plate scale and field of view (FOV) varied from run to run. Table 5.1 summarizes these details. It should also be noted that the detector read noise during observations ( $20\text{-}30\text{ e}^-$  CDS) was significantly higher than what we have obtained in recent laboratory measurements ( $8\text{-}10\text{ e}^-$  CDS).

Table 5.1: Details for observing runs at Kitt Peak 2.1m Telescope.

	Run 1: H4RG-10-007	Run 2: H1RG-022	Run 3: H2RG-32-147
Dates	4/24-4/30	11/13-11/19	12/12-12/19
Plate Scale	$0.126''/\text{pix}$	$0.227''/\text{pix}$	$0.227''/\text{pix}$
Field Of View	$8.5' \times 8.5'$	$3.8' \times 3.8'$	$7.5' \times 7.5'$
Photometric Nights	6	5	4
Electronics	SIDECAR	SIDECAR and ARC	SIDECAR
Guide Mode	No	No	Yes



Figure 5.1: A photograph of the RIDL dewar mounted to the Kitt Peak 2.1m telescope.

The detector was housed inside the RIDL dewar and positioned behind a filter wheel with six positions controlled by Phytron motors. One position was left open, one had an  $\text{Fe}^{55}$  source, one was a blank that prevented light from reaching the detector, and the other three were occupied by  $g$ ,  $i$ , and  $y$  filters described in Table 5.2. To accommodate the RIDL dewar, the telescope guider camera was removed from the telescope. The telescope was set to track at the sidereal rate and a rotator was used to correct for rotations of the field of view. The only exception to this was when H2RG-32-147 was operated in guide mode to simultaneously guide the telescope and take long exposures. In all, nearly 2 Terabytes of calibration and science data were collected in single window, multiple window, full frame, and guide mode. The majority of targets were chosen primarily to verify that HyViSI detectors can indeed function as astrometric and photometric instruments. Open clusters and bright stars from the SAO and GSC catalogs were used to test guide mode and measure persistence. And lastly, select Messier and NGC objects were targeted for tri-color imaging.

Table 5.2: Filter Characteristics

Filter Name	Peak (nm)	Cuton (nm)	Cutoff (nm)	Transmission (%)
$g$	476	401.22	557.87	96.39
$i$	742	667.61	815.77	96.14
$y$	1003	970.54	1036.01	86.28

## 5.2 Data Reduction and Calibration

As mentioned in Chapter 1, optical astronomers and astrophysicists are most familiar with CCDs. Even if they do not understand all of the steps in the signal chain or the technical details of how their sensor turns photons into a digital number, they at least know that certain steps must be performed to remove from the data as much of the CCD signature as possible. This process of cleaning the data and removing the instrumental signature is referred to as *data reduction*. Its real aim is to *reduce* all extraneous components of the data as much as possible so that what is left is pure signal.

It is beyond the scope of this thesis to present an adequate treatment of data reduction. Many excellent references are devoted to the subject. McLean gives a superb overview of the theory behind data reduction for non-destructive detectors [4]. Bushouse et al. provide a very detailed description of the data pipeline used to reduce exposures from the NICMOS infrared camera on Hubble [44]. Here we present only the basic theory and the steps needed to turn a set of raw astronomical images into a finished product that can be used for scientific study.

### 5.2.1 Data Reduction Theory

Because of the non-destructive readout of hybrid CMOS detectors, the reduction of the data is quite different from that of a CCD. In fact, it is more akin to data reduction for IR detectors. For a CCD, the data output of a single exposure is a two-dimensional set of pixel intensities  $I(x, y)$ . In contrast, for an up-the-ramp exposure as described in Section 3.1, the data output is in general a three-dimensional *data cube* with pixel intensities  $I(x, y, r)$ . The third dimension,  $r$ , is the read number and corresponds to the time at which the pixel at  $x, y$  was sampled. If the detector is reset and clocked in a uniform fashion with a frame time of  $t_{frame}$  then the times at which a pixel is sampled relative to the time it was reset are given by  $t(r) = t_{frame} * r$ .<sup>1</sup> The total number of reads  $R$  can vary from 1 to any greater integer, but an exposure with  $R = 1$  is rarely used in scientific applications because it is dominated by reset noise and pixel to pixel transistor current offsets.

Each sample of the datacube represents the measurement of an analog voltage  $V_{out}$  that has made its way from the pixel to the output of the detector. The voltage is proportional to the amount of charge integrated on the pixel capacitance from dark current, photo-current, and other sources such as carriers emitted from traps or released by minimum ionizing particles or radiation passing through the detector. Each of these carrier generating processes contains noise. This noise adds to the other noise contributors such as the Johnson noise of electrical currents passing through each of the transistors in the signal path and the ones described in Section 4.4. The voltages of the pixels will also each have their own equilibrium offset from ground due to subtleties such as the precise

---

<sup>1</sup>Note that for a given reset scheme  $t(r) = t_{frame} * r + t_{offset}$ . If the reset is applied pixel by pixel as the rows are clocked, then  $t_{offset} = 0$ . If the reset is applied to a whole row at a time, then  $t_{offset} = t_{pix} * n_{col}$ , where  $t_{pix}$  is the pixel time and  $n_{col}$  is the pixel column number relative to the first pixel in the row of the output channel to which it belongs.

values of  $N_A$  and  $N_D$  in the pixel implants, traps in the pixel source follower channel, proximity to current carrying buses, etc. The term *bias* is often used to describe this offset, although care must be taken to distinguish this from the case where it is used to describe *bias* voltages. In general, we can write the measured voltage as:

$$V_{out}(x, y, r) = V_{lum}(x, y, r) + V_{dark}(x, y, r) + V_{spurious}(x, y, r) + V_{bias}(x, y) + V_{noise\ det.}(x, y, r) \quad (5.1)$$

where

- $V_{lum}$  is the contribution from signal charge integrated due to light falling on the pixel. This is the signal of interest in astronomy.
- $V_{dark}$  is the contribution from charge integrated due to thermal leakage currents in or around the pixel.
- $V_{spurious}$  is the contribution from charge integrated as a result of trap emission or capture, persistence, overflow from neighboring pixels, x-ray and cosmic ray events, etc.
- $V_{bias}$  is the equilibrium offset voltage after the pixel has been reset.
- $V_{noise\ det.}$  represents all sources of noise between the pixel and the detector output. This term includes coupling to neighboring pixels as well as inductive or capacitive pickup from other current carrying buses on the detector.

The first three terms in Equation 5.1 are related to the charge that has accumulated in the pixel,  $Q(x, y, r)$ , by the gains described in Section 4.3. That is,  $V(x, y, r) = Q(x, y, r)/(G_{PIXEL} * G_{UC} * G_{OUT})$ . The last two terms cannot be as easily related to measurable quantities. For instance,  $V_{noise}$  might include pickup from a ground loop on the detector, which could vary wildly in different configurations and is extremely difficult to pinpoint.

The pixel intensity that is stored in the datacube is a sample of the analog voltage recorded by the control electronics. The electronics and sampling process itself imparts a noise  $V_{noise\ elec.}$  on the signal (see Section 3.5), and in addition, amplifies  $V_{noise\ det.}$  by the electronics gain  $G_{AMP}$ . Since the noise component from the detector and the one from the control electronics are, at least in principle, uncorrelated, they add in quadrature:

$$V_{noise} = \sqrt{G_{AMP}^2 V_{noise\ det.}^2 + V_{noise\ elec.}^2} \quad (5.2)$$

This expression effectively replaces  $V_{noise\ det.}$  in Equation 5.1. With all voltage contributions taken

into account, the ADC converts the sum to a digital number,  $I$ , in Analog-Data-Units (ADU):

$$I(x, y, r) = G_{A/D} \left[ G_{AMP} (V_{lum}(x, y, r) + V_{dark}(x, y, r) + V_{spurious}(x, y, r) + V_{bias}(x, y)) + \sqrt{G_{AMP}^2 V_{noise\ det.}^2(x, y, r) + V_{noise\ elec.}^2} \right] \quad (5.3)$$

Note that here we are using  $G_{A/D}$  in units of ADU/ $\mu$ V.

After conversion the pixel values are transmitted to a computer for storage. In astronomical applications, the most commonly used storage format is the Flexible Image Transport System (FITS). For the data collected for this thesis with the SIDECAR and ARC electronics, the pixel values were stored as datacubes of 16-bit unsigned integers in FITS format.

The digital pixel values are often called the *raw data*, and it is with these values that data reduction is performed. A fundamental assumption is that each of the terms in Equation 5.3 are independent of one another. For instance, the assumption is made that  $V_{dark}(x, y, r)$  is the same whether or not light is falling on the detector. With this being the case, an exposure taken in the dark can be subtracted from an illuminated exposure to remove the dark current component along with any well behaved, time-dependent noise sources. Another assumption is that certain noise components are Gaussian distributed. Thus, they can be beaten down by taking multiple exposures with the same  $V_{lum}$ . While these techniques and many others apply to both CCD and CMOS sensors, the fact that a typical CMOS exposure contains multiple samples of a time-dependent signal gives rise to some important differences. The data volume is in general much larger, saturated pixels can still yield flux estimates, and the signal can be measured as a rate of change of light falling on the detector or as a total of the integrated light. The following sections present a short list of data reduction techniques in the context of hybrid CMOS detectors.

### 5.2.2 Reference Pixel Correction

The reference pixels of the HxRG multiplexers provide an excellent means for reducing common mode noise in the detector. A thorough description of them is given in Section 3.4. For each read in the datacube, the average of the left set of reference pixels ( $i = 0, 1, 2, 3$ ) and the average of the right set of reference pixels ( $i = N - 3, N - 2, N - 1, N$ ) is taken across the rows to yield two one dimensional column vectors:

$$S_{ref\ l}(j, r) = \sum_{i=0}^3 \frac{S(i, j, r)}{4} \quad S_{ref\ r}(j, r) = \sum_{i=N-3}^N \frac{S(i, j, r)}{4}, \quad (5.4)$$

where  $N$  is the number of pixels in a detector row. A Savitsky-Golay filter is then used to smooth the columns and yield the two vectors  $\hat{S}_{ref\ l}$  and  $\hat{S}_{ref\ r}$ . Finally, the smooth vectors are multiplied

by the factor  $C_{FAC}$  and subtracted from the science pixels belonging to their respective half:

$$S(i, j, r) = S_{sci}(i, j, r) - C_{FAC} * \hat{S}_{ref} \quad (5.5)$$

The subtraction of the reference pixels will effectively boost the read noise by  $\sqrt{2}$ . In some cases, this number will be small compared to bias voltage drifts or  $1/f$  noise. In other cases the reference pixels will not show any drift at all. The stability of the common mode noise has a very complex dependence on the state and history of all operating conditions: temperature, bias voltages, substrate voltage, clocking patterns, etc. Subtraction of the reference pixels should therefore be made on a case by case basis.

### 5.2.3 Dark Subtraction

To remove the contribution from dark current,  $V_{dark}(x, y, r)$ , we first obtain a series of dark ramps having the same cadence as the ramps we wish to reduce (see Section 3.1.1 for a definition of *cadence*). We then take the median of each pixel value at each read across the exposures to yield a median dark datacube with pixel values  $I_{dark}^{med}(x, y, r)$ . The median filter efficiently rejects cosmic rays and voltage spikes, but a mean filter with outlier rejection can be applied instead to improve the signal estimation. It is extremely important that the bias read ( $r = 1$ ) of each exposure be subtracted from each of the subsequent reads in that same exposure to remove *kTC* noise **before the median filter is applied**. In other words, for the  $j$ th dark exposure:

$$I_{dark}^j(x, y, r) = I_{dark}^j(x, y, r) - I_{dark}^j(x, y, r = 1) \quad (5.6)$$

This can usually be done with the stored values in computer memory before the median is applied as long as the datacubes are sufficiently small. Note that the frame  $I_{dark}^{med}(x, y, r = 1) = 0$  and can be discarded from the median dark datacube to save disk space.

From each illuminated (object) ramp through a given filter we subtract the median dark ramp:

$$I_{obj}(x, y, r) = I_{lum}(x, y, r) - I_{dark}^{med}(x, y, r), \quad (5.7)$$

where  $I_{lum}$  is the pixel value from the illuminated image. The bias read  $I_{obj}(x, y, r = 1)$  will remain the same, but the dark current contribution to each subsequent read will be removed. The resulting frames in this ramp should, in theory, have pixel values,  $I_{obj}$ , that correspond to luminance from the source being observed.

### 5.2.4 Slope Fitting

The next order of business is to estimate the photocurrent for each pixel ramp in the datacube of interest:  $I_{obj}$ . As discussed in Section 4.4.2.4, fitting a slope to the ramps is a good technique for

this since it beats down the read noise and aids in cosmic ray rejection. Plus, it is assumed that this data reduction is being performed on a computer dedicated for analysis, so processing complexity and memory should not be a critical issue.

The slopefit should only be applied to the ADU values for which the pixel ramp is linear. According to the discussion in Section 4.7, the ramps will take on a nonlinear behavior when the pixel well is near capacity, and this transition will take place at some upper limit in the *raw* signal,  $I_{lum}^{max}$ . Nominally, a value  $I_{lum}^{max}(x, y)$  for each pixel would be used, but a mean value can also be used without a noticeable reduction in the quality of the slopefits. One may also prescribe some lower value  $I_{lum}^{min}(x, y)$  below which the signal is not considered for a slopefit, perhaps because of some nonlinearity in the early reads. Once these limits have been prescribed, we consider the ADU values in between to be in the *linear regime*.

In order to find the slope that minimizes the error for the points in the linear regime, i.e. where  $I_{lum}$  lies between  $I_{lum}^{min}$  and  $I_{lum}^{max}$ , we fit a line to the corresponding values of  $I_{obj}$  using the technique described in Numerical Recipes [82]. Namely, for a pixel that has  $N_{rd} = r_{max} - r_{min}$  values of  $I_{lum}(r)$  between reads  $r_{min}$  and  $r_{max}$ , and corresponding dark subtracted values  $I(r) = I_{obj}(r)$ ,

$$b = \frac{\sum_{r_{min}}^{r_{max}} t(r)^2 \sum_{r_{min}}^{r_{max}} I(r) - \sum_{r_{min}}^{r_{max}} t(r) \sum_{r_{min}}^{r_{max}} t(r) I(r)}{N_{rd} \sum_{r_{min}}^{r_{max}} t(r)^2 - (\sum_{r_{min}}^{r_{max}} t(r))^2}$$

$$m = \frac{N_{rd} \sum_{r_{min}}^{r_{max}} t(r) I(r) - \sum_{r_{min}}^{r_{max}} t(r) \sum_{r_{min}}^{r_{max}} I(r)}{N_{rd} \sum_{r_{min}}^{r_{max}} t(r)^2 - (\sum_{r_{min}}^{r_{max}} t(r))^2}. \quad (5.8)$$

$b$  is an approximation to the bias offset in ADU, and  $m$  is the number of ADU/s attributed to the source of illumination. It should be apparent that only the difference in times  $t(r)$  and  $t(r+1)$  matters, so it suffices to use the average time for the  $r$ th read. With a slope obtained and the proper conversion gain in  $e^-/\text{ADU}$ ,  $m$  can be converted to units of  $e^-/\text{s}$ .

Bright objects will induce saturation very quickly, and in some cases there will be too few or no values of  $I_{lum}(r)$  in the linear regime. These cases require alternative approaches. If a pixel is saturated in the second read (the bias read is considered the first read) and  $I_{lum}(1) < I_{lum}^{max} - 0.5I_{lum}^{FR}$ , where  $I_{lum}^{FR} = I_{lum}^{max} - I_{lum}^{min}$ , the slope is approximated by the CDS value  $m = (I(2) - I(1))/(t(2) - t(1))$ . And if a pixel is saturated in the second read and  $I(1) > I_{lum}^{max} - 0.5I_{lum}^{FR}$ , the best one can do is approximate the slope by  $m = I(1)/t(1)$ .

Once a slope has been fit to the points in the linear regime, cosmic rays are detected as large deviations from the fit using the same method as the one in the NICMOS reduction code [44]. In this method, the difference between the data points and the fit is first computed as

$$D(r) = I(r) - (m \cdot t(r) + b). \quad (5.9)$$

Then the difference between adjacent points in this difference is taken,

$$DD(r) = D(r) - D(r - 1), \quad (5.10)$$

along with its standard deviation,  $\sigma_{DD}$ . Cosmic rays are flagged as points where  $DD(r) > T_r \sigma_{DD}$ , where  $T_r$  is some threshold. For our HyViSI data,  $T_r$  was typically set around 3. The idea behind this scheme is that the cosmic rays particles will release significantly more charge in the pixel over some small time interval than the integrating photocurrent and show up as a large negative to positive spike in  $D_i$ . Using a separate  $\sigma_{DD}$  for each individual pixel seems to be quite effective and well suited for treating the variation in pixel sensitivity across the array.

Ideally, if a cosmic ray is detected in a read  $r = r_{cr}$  late in the ramp,  $r_{cr} > r_{min} + N_{rd}/2$ , then the slope is refit using points from  $r = r_{min}$  to  $r = r_{cr}$ . And if it is detected early in the ramp,  $r_{cr} < r_{min} + N_{rd}/2$ , the slope would be ideally refit using points  $r = r_{cr}$  to  $r = N_{rd}$ . However, the latter results in extremely large error for nearly all of the HyViSI devices tested for this thesis due to IPCT (see Section 6.1.2), and so the beginning of the ramp must be used instead. After refitting, the number of points used in the fit after the cosmic ray rejection should be included as an extension to the image for purposes of error analysis.

An added benefit of UTR sampling is that the energy deposited by a high energy particle can be well approximated by examining the signal  $I_{r_{cr}} - I_{r_{cr}-1}$ . These values can be recorded and stored as a separate image. They are potentially interesting for measuring the angular distributions, frequency, and morphology of such events.

### 5.2.5 Flat Fielding

After every pixel has had a slope fit to it for the object exposure, we are left with an NAXIS1×NAXIS2 array of slopes,  $m_{obj}(x, y)$ , that we take to be the image. To account for the pixel to pixel variations in sensitivity—this can be due to small differences in the gain between individual pixels, dust on the detector, vignetting, etc.—we must apply a flat field.

Flat field exposures are recorded while the detector is uniformly illuminated through the appropriate filter. The light level should be great enough so that vignetted pixels see a reasonable photocurrent and the cadence should be chosen so that the pixels do not oversaturate. As mentioned in Section 4.6.2, the illumination setup used for the flats should be as close to that for the object exposures as possible in order to account for fringing at wavelengths near  $1 \mu\text{m}$ . If the incoming rays are not oriented similarly in the two, the fringes will appear in different spatial locations. As an example of this, during our telescope observations we collected both “dome” flats where we exposed the detector to a uniformly lit white spot on the interior of the telescope dome and “sky” flats where we exposed the detector to the sky at twilight. The “sky” flats, which are clearly more representative of the illumination delivered by the parallel rays coming from the night sky, were far

more successful in removing the fringes than the dome “flats”, where the rays entering the telescope optical system cannot be considered parallel due to the proximity of the source to the primary mirror of the telescope.

After recording a sufficient amount of flat field exposures, a median flat is generated in the same way that the median dark was formed (i.e. the bias reads are subtracted from the individual exposures and then the median is obtained). Then, the median dark is subtracted and slopes are fit to the pixel ramps in the median flat according to the method described in Section 5.2.4, which yields a 2-d image that we call  $m_{flat}(x, y)$ . For simplicity, at this point  $m_{flat}(x, y)$  is normalized so that the values range from 0 to 1. Finally, the flat is applied to the object image by dividing the slopes:

$$m_{fin}(x, y) = \frac{m_{obj}(x, y)}{m_{flat}(x, y)}, \quad (5.11)$$

to yield the final slopes  $m_{fin}(x, y)$ .

One important consideration to keep in mind when recording darks and flats with the HyViSI detectors is that persistence in flat field images will show up in dark current measurements. Therefore, it is very important that the dark exposures are either recorded before the flat fields or sufficient time is given for any persistence to subside before recording the darks.

### 5.2.6 Combining Dithers

Dithering is a very useful technique for eliminating the impact of bad pixels or regions of defects on the detector. In the majority of cases, for our *full frame* exposures we used a dithering technique to provide a number of samples of each field, each of them being slightly offset from the others in terms of location on the detector. The dither pattern was a  $3 \times 3$  box where each telescope pointing was offset from the previous one by  $20''$  ( $\sim 160$  pixels on the H4RG and  $\sim 80$  pixels on the H1RG or H2RG). A full exposure was taken at each of these pointings, yielding 9 or more slopefitted images of the field in each filter depending on whether or not the dithering sequence was repeated.

The flat-fielded slope images,  $m_{fin}(x, y)$ , from each filter are aligned using several bright stars and then combined into a mosaic. To combine the data from the multiple pixel values at a spatial location (x,y) in mosaic image coordinates, we use both a median filter and the mean of the pixels that were not flagged as bad or rejected as  $3\sigma$  outliers. The mean provides a slightly better reduction in noise, and the mean mosaics are the images that we use for analysis in the following sections.

### 5.2.7 Telescope Calibration with Multiple Windows

High speed photometric measurements of the Delta Scuti star BE Lyn ( $V \sim 8.8$ ) were made during the observing run with H2RG-32-147. On the night of December 17, 2007, BE Lyn and the nearby reference star GSC 03425-00544 ( $V \sim 11.1$ ) were simultaneously imaged at a rate of 4 Hz over the course of several hours. The two stars are separated by approximately  $2'$ . A separate  $61 \times 61$  guide

window was used for each star, in a sequence where the first and second windows were reset in series, read once in series, and read once again in series to provide a Correlated Double Sample (CDS). This sequence was executed repeatedly and was only interrupted when it was necessary to write the data to a FITS file. In addition to providing temporal flux measurements, from which the period of BE Lyn was measured in  $i$  band (see Section 5.3.4), this data inadvertently provided a detailed look at the telescope tracking.

The star centroids calculated from this data show that there are significant tracking errors for both right ascension and declination. In fact, the errors were so large that it was necessary to manually offset the telescope while the observations were being made. This was possible since the data was being displayed in real time on a computer monitor. The errors are quantified as *drifts* between the telescope tracking rate and the sidereal rate. For periods of about 20 minutes or less, the drift in DEC can be fit with a straight line; any longer than this and a curvature becomes evident, especially as the telescope crosses the meridian. The drift in RA has both a long period linear component and a short period sinusoidal one. The drifts  $\Delta_{DEC}$  and  $\Delta_{RA}$ , measured in arcseconds, can be reasonably well fit over time-spans less than 20 minutes with the functions:

$$\begin{aligned}\Delta_{DEC} &= m_{DEC} * t \\ \Delta_{RA} &= m_{RA} * t + A \sin(2\pi f_{osc} t),\end{aligned}\tag{5.12}$$

where  $m_{DEC}$  and  $m_{RA}$  are the linear slopes of the drifts, and  $A$  and  $f_{osc}$  are the amplitude and frequency of the short period oscillation in RA, respectively.

For 12 piecewise fits over the 4 hour time span, the average slopes were found using least square fits to the data. The magnitude of  $m_{RA}$  varied between 0.110"/minute and 0.950"/minute, and was greatest right before crossing the meridian. The sign of  $m_{RA}$  was always negative, indicating that the telescope was lagging the movement of the sky. The sign of  $m_{DEC}$  changed several times over the 4 hour period. Its magnitude ranged from 0.028 "/minute to 0.39 "/minute, and was also largest while the telescope crossed the meridian.

After removing the linear component in the RA data, a discrete Fourier transform of its autocorrelation was performed for each piecewise fit. The frequency was determined to be  $f_{osc} = 0.00833$  Hz, corresponding to a period of 120 seconds. This frequency was extremely consistent throughout the data and so was the value of the amplitude,  $A = 0.5104''$ . Although the residuals in the fit show that the oscillations are not purely sinusoidal (more time is spent in the leading portion of the curve than the lagging portion), the amplitude and frequency provide an estimate on the reduction in image quality. A fit to the data for a 16 minute period is shown in Figure 5.2. It should also be noted that autocorrelations in the DEC drift show power at  $f_{osc}$ , indicating that the two coordinate motions are coupled. However, the amplitude is much lower, at about the level of the high frequency components induced by atmospheric effects.

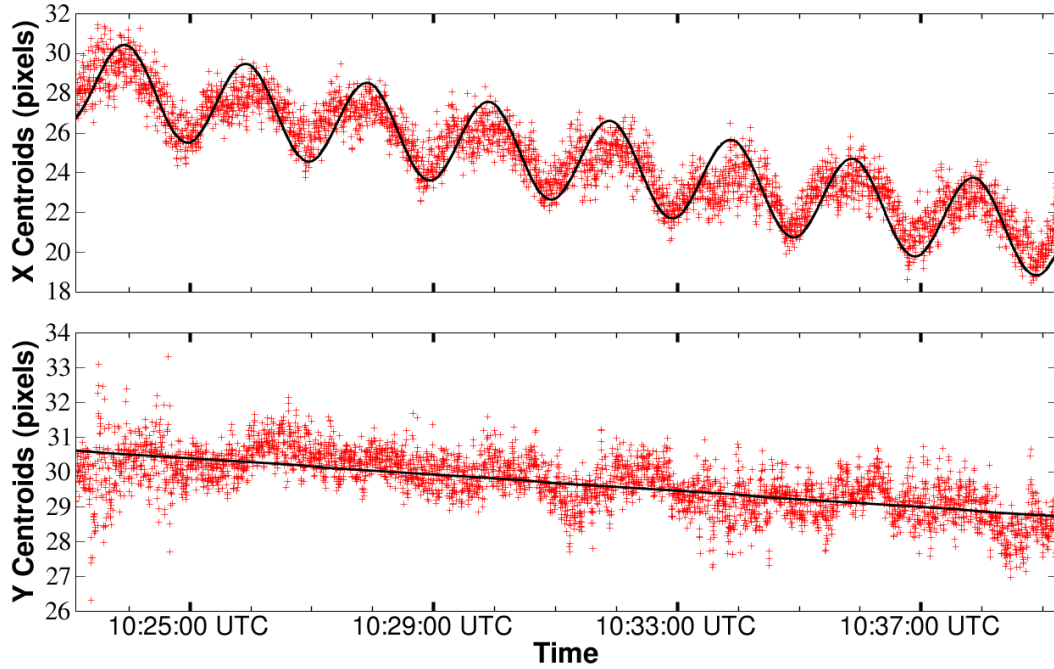


Figure 5.2: The telescope drifted significantly over a 20 minute period and showed sizable oscillations without the assistance of a guider. The centroids from images taken at 4 Hz are shown as plus marks. The black lines show the fits to the drifts from Equation 5.12 with  $m_{RA} = -0.108''/\text{minute}$ ,  $m_{DEC} = -0.026''/\text{minute}$ ,  $f_{osc} = 0.00833 \text{ Hz}$ , and  $A = 0.5104''$ .

### 5.2.8 Expected Point Spread Function

The tracking error functions in Equation 5.12 can be used directly to predict the image quality for unguided and guided exposures. The full data set collected during the observing runs with H1RG-022 and H2RG-2-147 shows that the system point spread function (PSF) is Gaussian and seeing-limited for intermediate length exposures (long enough to average out atmospheric turbulence and short enough to avoid degradation from tracking error). For long exposures, the center of the Gaussian profile is assumed to drift at the rates  $m_{DEC}$  and  $m_{RA}$  in DEC and RA, respectively, and oscillate in RA at a frequency of  $f_{osc}$ . For an exposure of length  $t_{exp}$ , the resulting point spread function will thus be:

$$I(x, y) = \int_0^{t_{exp}} I_o \exp \left( \frac{-(x - m_{RA} * t - A \sin(2\pi f_{osc} t))^2}{2(\epsilon/2.35)^2} + \frac{-(y - m_{DEC} * t)^2}{2(\epsilon/2.35)^2} \right) dt, \quad (5.13)$$

where  $\epsilon$  is the Full Width at Half Max (FWHM) due to the average seeing in arcseconds, and  $I_o$  is the peak intensity of the stellar image. Numerical solutions to this integral were obtained for representative values of  $\epsilon$ ,  $t_{exp}$ ,  $m_{RA}$ ,  $m_{DEC}$  in order to predict the image quality in both guided

and unguided operation.

To quantitatively describe the PSF for each solution, a  $21 \times 21$  box around the centroid of the intensity distribution is used to compute the second moments  $I_{xx}$ ,  $I_{yy}$ , and  $I_{xy}$ , where:

$$I_{ij} = \frac{\sum_{n,m} x_i(n,m)x_j(n,m)I(n,m)}{\sum_{n,m} I(n,m)}. \quad (5.14)$$

From these, the ellipticity vector is calculated from its components,  $e_1$  and  $e_2$ , according to the prescription in Bacon et al. [83]:

$$e_1 = \frac{I_{xx} - I_{yy}}{I_{xx} + I_{yy}}, \quad e_2 = \frac{I_{xy}}{I_{xx} + I_{yy}}. \quad (5.15)$$

The magnitude of ellipticity,  $e$ , and its angle,  $\theta$ , are given by

$$e = (e_1^2 + e_2^2)^{1/2}, \quad \tan 2\theta = e_2/e_1. \quad (5.16)$$

In addition to these measurements, the radial profiles around the centroid are fit with one-dimensional Gaussian and Moffat functions. The FWHM from the fits, along with the second moments, measure the overall extent of the PSF, while the ellipticity measures the asymmetry in RA and DEC. Together these quantities adequately describe the PSF.

### 5.2.8.1 Unguided Operation

It is fairly straightforward to see from Equation 5.12 that if the telescope is not guided, the tracking errors will quickly produce a PSF that is broadened beyond the seeing disc and elongated along the direction of the drift. However, it is not trivial to quantitatively describe the effect the drift will have on its shape. For two representative drift rates observed during the photometric measurements of BE Lyn, the ellipticity and FWHM obtained from a Gaussian fit were calculated for a range of atmospheric seeing values,  $\epsilon$ , assuming  $t_{exp} = 1800$  s. The results are shown in the top two curves of Figure 5.3.

The plots show that the ellipticity can easily exceed 0.2 when the blurring due to seeing is not large enough to mask the sinusoidal oscillation and drift of the telescope. This effect is more pronounced when  $m_{RA} > m_{DEC}$  since the centroid motion along the x axis of the detector is far greater than the motion along the y axis during the exposure. It should also be noted that at a given value of  $\epsilon$  the ellipticity will be an increasing function of  $t_{exp}$ , as the smearing along the direction of drift increases, while in the transverse direction it remains constant. For short exposures ( $t_{exp} < 1$  m), a Gaussian shape is preserved for typical seeing values.

### 5.2.8.2 Guided Operation

During our last observing run we implemented guide mode with H2RG-32-147 (results are shown in Section 5.5) and issued offsets to the telescope to correct for tracking error. In our configuration, one set of IDL scripts was used to collect data from the SIDECAR ASIC through its USB interface and another set of IDL scripts communicated to the Telescope Control System (TCS) via a RS-232 serial port connection. Centroids were calculated from the guide window data in IDL as the other detector pixels were integrating up the ramp, and an offset was issued to the telescope if it appeared that the telescope was drifting.

The TCS for the 2.1m accepts offsets as small as 0.1 arcseconds. However, due to telescope motor hysteresis and other mechanical effects, the minimum offset which can be issued with precision is not this small. While a precise value is not known, it is definitely less than 1 arcsecond. After some initial measurements, we found that the best results were obtained when we issued offsets only if the centroid of the star had moved by  $0.3''$ , which corresponds to about 1.3 pixels with the  $0.232''$  plate scale. On average we found that an offset in RA was needed every 20-50 seconds. The declination adjustment varied between once per 1-5 minutes depending on the altitude of the pointing.

To predict the quality of the PSF with the adjustments described, Equation 5.12 is not used directly. Instead, it is broken up into a total of  $t_{exp}/t_{min\ adj.}$  separate integrals, where  $t_{min\ adj.} = 20$  s is the interval of time between the most frequent adjustments in *RA*. For each integration, the center in *x* of the Gaussian is set back to zero. The center in *y* is set back to zero only at the end of a time interval  $t_{max\ adj.} = \alpha t_{min\ adj.}$ , where  $\alpha$  represents the ratio of *RA/DEC* adjustment frequencies. This number ranged between 3 and 15 depending on the pointing. The phase of the sinusoidal motion is preserved between successive integrations to best represent the observed behavior of the telescope motion after small adjustments.

The results of calculations for which  $t_{min\ adj.} = 22$  s,  $\alpha = 12$ , and  $t_{exp} = 1800$  s are shown in the bottom two curves of Figure 5.3. The linear drift rates are the same as the two cases represented in the unguided calculation. The ellipticity and FWHM are greatly diminished as expected. However, the asymmetric centroid motion along the *x* and *y* axes yields a nonzero ellipticity. For small linear drift rates, the sinusoidal motion along the *x*-axis is actually the greatest contributor. This can be understood by considering the times immediately after the telescope has been corrected in *RA*. Since the phase of the oscillatory motion is preserved after adjustment, the pointing of the telescope following a correction will in some cases swing in the opposite direction of the linear motion and contribute to a greater blurring in the *x* direction.

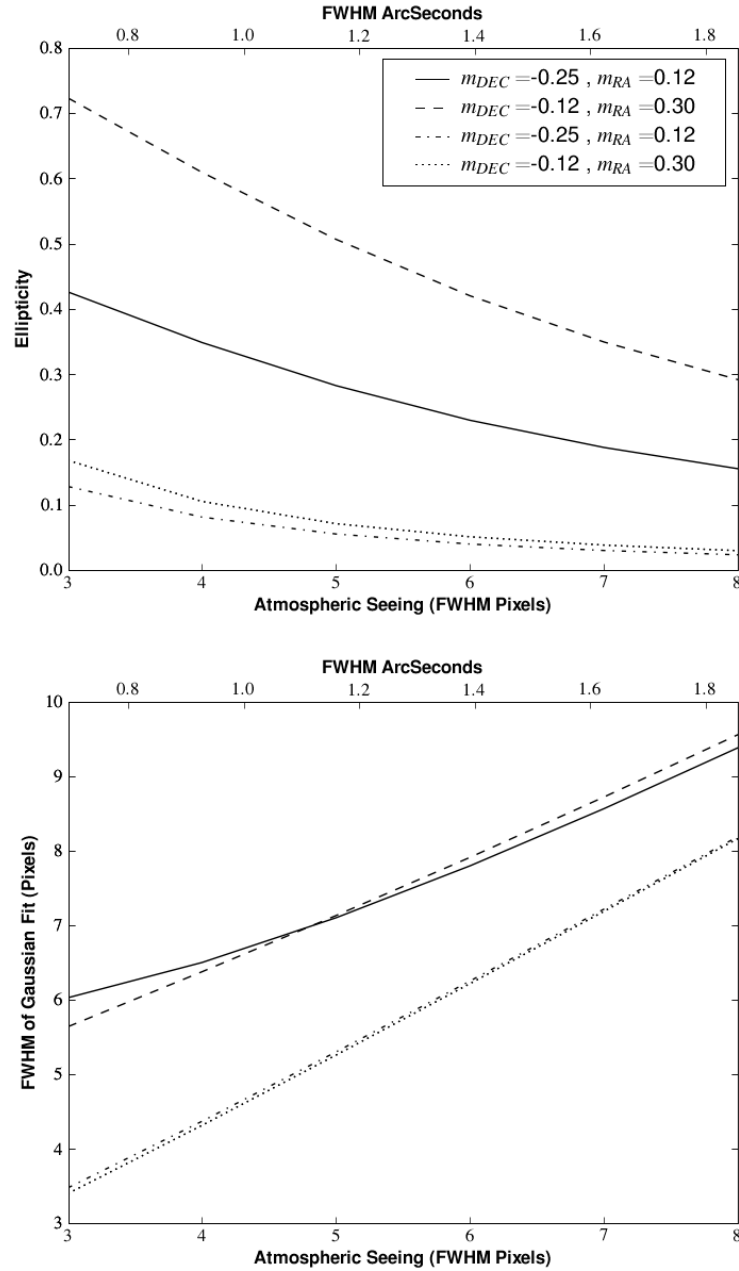


Figure 5.3: Expected ellipticity (top) and FWHM (bottom) derived from a Gaussian fit with a drifting center for a 30 minute exposure. The drift rates  $m_{DEC}$  and  $m_{RA}$ , expressed in  $''/\text{minute}$  are shown in the legend. The top two curves in each plot represent the results for the cases where the telescope is allowed to drift. The bottom two show the calculation results for the cases where the drift is corrected (by re-centering the Gaussian) whenever the pointing has exceeded  $1.3''$  in  $RA$  or  $DEC$ , as was the case during our guiding operation.

### 5.3 Photometry

In an astronomical context, photometry is the measurement of celestial source brightnesses.<sup>2</sup> While the traditional practice of expressing these brightnesses in *magnitudes* is still favored in astronomy, for astrophysical purposes, the end goal of *absolute photometry* is to relate them to the amount of energy emitted by a particular object per unit time per unit area, A.K.A. the flux. The practical way to do this with a particular instrument is to observe a well measured standard star and use *relative photometry* to convert between the instrumental measurements and an absolute scale. Even with this *apparent* flux, though, the distance to the object must be known to obtain the *absolute* flux. In general, the brightnesses are measured over a wavelength bandpass that is relatively large in comparison to the wavelength itself, e.g. through color filters for visible wavelengths. When the bandpasses become sufficiently small and a number of them are used, one enters the realm of spectrophotometry. Photometry is undoubtedly one of the most important areas of astronomy; our understanding of open and globular clusters, variable stars (which also provide distance estimates), supernovae, and a whole host of other phenomena would be nonexistent without it. As such, it is essential that an astronomical detector be capable of delivering accurate photometric measurements.

Since the CCD entered into the arena of astronomy, it has been the “undisputed leader” in photometry [84]. The CCD is superior to photographic emulsions because of its high quantum efficiency and large dynamic range, and highly more efficient than an accurate photomultiplier tube because of its large field of view. In the past, the poor quantum efficiency and fill factor of CMOS detectors made them inferior to CCDs as well. However, with the advent of hybrid and back illuminated CMOS detectors, a comparative study between photometric performance of CCD and CMOS detectors is now a legitimate one. In fact, if CMOS detectors can match the photometric accuracy of CCDs, they will be inherently better in the fast time domain because of the windowing capability and fast readout speed.

To assess the potential of the HyViSI detectors as photometric instruments, several studies were carried out. These included aperture photometry on well calibrated photometric sources (Landolt stars), crowded-field photometry of globular clusters, and high speed window photometry of variable and multiple sources. Each of these illustrates the ability of the detector to operate in a different photometric regime.

Photometric measurements of Landolt stars are well suited for testing the ability of the detector to sense brightness differences within a particular wavelength passband as well as determining how well the detector can be calibrated to obtain absolute magnitudes within that band. Crowded-field photometry of the stars in M13 is good for determining the spectral responsivity of the detector by comparing measurements through separate passbands since the relationship of color index vs. magnitude has been well studied in the cluster. And lastly, fast measurements in window mode

---

<sup>2</sup>Technically, there is a distinction between *photometry*, which applies to the visible wavelength range, and *radiometry*, which applies to the entire spectrum. In practice, astronomers use the former term to describe both.

provide an indication of how well the detector can sense changes in illumination. In the following sections, each will be described in turn.

### 5.3.1 Aperture Photometry

Landolt Standard stars provide a good set of basis measurements for comparison as they have been repeatedly observed through different filter sets with different calibrated instruments. With H4RG-10-007, instrumental magnitudes of well isolated standard stars in the Landolt Equatorial Fields PG 1530 and SA 109 were obtained. Unfortunately, these standards have been observed very frequently through UBVRI filters of the Johnson-Kron-Cousins system, but not through  $g, i,$  and  $y$  filters that are more closely matched to our set. It is possible, however, to make a transformation between pairs of filters in these two systems under the assumption that the variation of the spectral energy distribution  $E(\lambda)$  of the stars is sufficiently continuous over the intervals considered to allow a Taylor expansion in  $\lambda$ .

Such a transformation is done, as in Verdoes et al. [85], by solving the following equations:

$$m_l^{H4RG} = M_j^{CAL} Z - KX + CT \times (M_k^{CAL} - M_j^{CAL}), \quad (5.17)$$

where  $M_j^{CAL}$  is the reference magnitude in the filters  $j = V, I,$  and  $Y,$   $m_l^{H4RG}$  is the instrumental magnitude that we measured through the filters  $l = g, i,$  and  $y,$   $X$  is the airmass,  $K$  is the atmospheric extinction coefficient,  $CT$  is a color coefficient and  $M_k^{CAL} - M_j^{CAL}$  is the color defined by filter  $j$  and  $k = B, R,$  and  $H$  from the reference measurements. Astronomers frequently use these equations in order to compare measurements made at different telescopes and to calibrate for slight differences between filter sets. They are typically solved using a population of several hundred standard stars. Due to limited time and data, we have only seven.

The transformations require a calculation of an average airmass over the duration of our exposures in each filter band. For this we used the algorithm suggested by Stetson [86] :

$$X_{avg} = (X_{beg} + 4X_{mid} + X_{end})/6, \quad (5.18)$$

where  $X_{beg}$  is the airmass at the beginning of the first exposure,  $X_{mid}$  is the airmass midway through the exposure (for us it was the fifth dither in the sequence) and  $X_{end}$  was the airmass at the end of the dither sequence. The average airmasses through which we observed ranged from 1.12 to 1.26, so loss due to atmospheric extinction was not very significant.

Once the equations are solved, they can be used to predict the magnitudes we should expect to observe for  $g, i,$  and  $y$  filters at zero airmass based upon standard magnitudes in  $V, I,$  and  $Y$  and the corresponding colors. The fitting coefficients and errors are shown in Table 5.4 and a plot that illustrates the goodness of the fit is shown in Figure 5.4. The errors in the fit are not unreasonable. They are similar to the ones found in the transformations made in the Sloan Digital Sky Survey [87].

The error in  $g$  is substantially higher than it is in  $i$  and  $y$ . This may be attributed to a number of factors including observing conditions, wavelength dependent lateral diffusion in the detector, and nonlinearity. The exact reason for the large discrepancy is still being investigated. However, the data and the fit indicate that H4RG-10-007 is capable of doing absolute photometry.

From a preliminary aperture photometry analysis of open cluster data obtained with H1RG-022 and H2RG-32-147, the photometric errors for these detectors are smaller than those for H4RG-10-007. This improvement in performance is expected since the dark current shot noise is significantly less in the H1RG and H2RG. Also, the reset voltages were tuned properly for observations with these detectors to prevent the nonlinear behavior we observed in the early reads of the ramps in H4RG-10-007. In the newest generation of H4RG, a large reduction in dark current is observed, suggesting that the photometric accuracy will be improved [88].

Table 5.3: Landolt Star Magnitudes. Our measured magnitudes are denoted by lowercase  $m$ .  $M$  are magnitudes taken from catalogs; + are taken from Landolt (1973)[89],  $\diamond$  are taken from Landolt (1992) [90], and  $\star$  from Gullixson (1995) [91]. All  $M_Y$  are from Persson (2002) [92].

Star	$M_Y^{CAL}$	$\Delta M_Y^{CAL}$	$M_Y^{CAL} Error$	$M_Y^{CAL} - M_H^{CAL}$	$m_y^{H4RG}$	$\Delta m_y^{H4RG}$	$m_y^{H4RG} Error$
109-956	12.516	0.000	0.029	1.038	15.362	0.000	0.001
109-954	10.254	2.262	0.028	1.064	13.079	2.283	0.001
109-949	11.384	1.132	0.029	0.595	14.250	1.112	0.001
	$M_V^{CAL}$	$\Delta M_V^{CAL}$	$M_V^{CAL} Error$	$M_B^{CAL} - M_V^{CAL}$	$m_g^{H4RG}$	$\Delta m_g^{H4RG}$	$m_g^{H4RG} Error$
109-959 $\star$	12.790	0.000	0.029	0.780	12.404	0.000	0.003
109-956 $\diamond$	14.639	-1.849	0.011	1.283	14.407	-2.003	0.009
109-954 $\diamond$	12.436	0.354	0.009	1.296	12.187	0.217	0.003
109-949 $\diamond$	12.828	-0.038	0.006	0.806	12.408	-0.004	0.002
1530-057 $\diamond$	14.21	0.000	0.000	0.151	12.756	0.000	0.003
1530-057A $\diamond$	13.71	0.500	0.000	0.829	12.514	0.242	0.003
1530-057B $\diamond$	12.84	1.37	0.000	0.745	11.595	1.161	0.002
	$M_I^{CAL}$	$\Delta M_I^{CAL}$	$M_I^{CAL} Error$	$M_R^{CAL} - M_I^{CAL}$	$m_i^{H4RG}$	$\Delta m_i^{H4RG}$	$m_i^{H4RG} Error$
109-959 +	11.572	0.000	0.009	0.671	12.197	0.000	0.003
109-956 $\diamond$	13.114	-1.542	0.016	0.743	13.886	-1.689	0.007
109-954 $\diamond$	10.940	0.632	0.003	0.731	11.391	0.806	0.002
109-949 $\diamond$	11.708	-0.136	0.003	0.517	12.422	-0.225	0.003
1530-057 $\diamond$	14.011	0.000	0.000	0.036	12.967	0.000	0.003
1530-057A $\diamond$	12.842	1.169	0.000	0.412	11.967	1.000	0.002
1530-057B $\diamond$	12.041	1.970	0.000	0.376	11.160	1.807	0.003

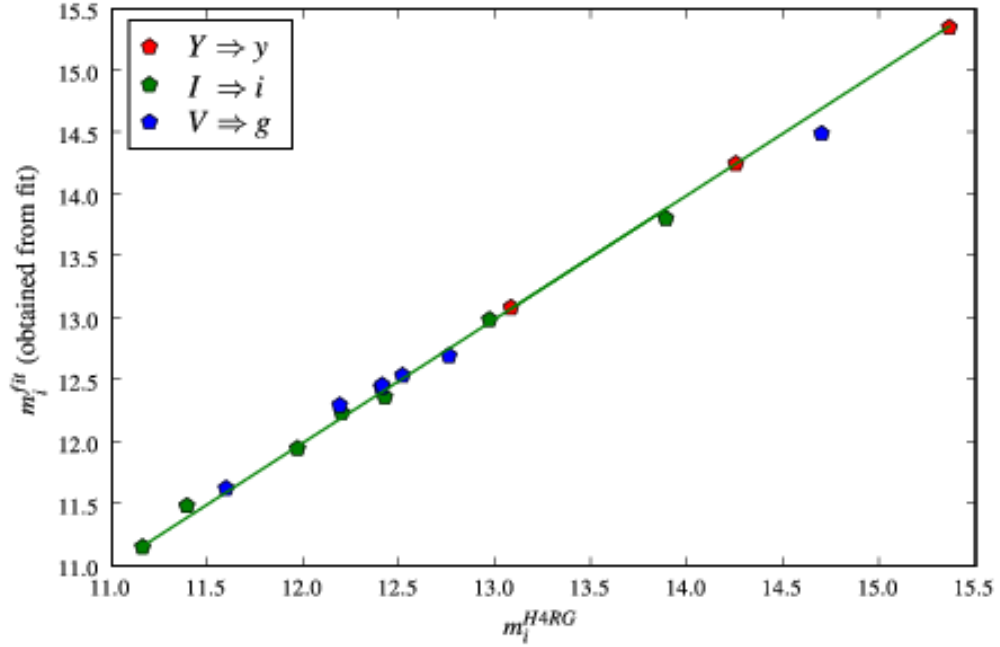


Figure 5.4: The results from the best-fit solution to the transformation equations. The horizontal axis shows the magnitudes that we measured in our images. The vertical axis shows the magnitudes that are expected from the fits in Table 5.4 based upon the standard magnitudes. The green line shows where  $m_i^{HARG} = m_i^{fit}$ .

Table 5.4: Transformation equations obtained from the data in Table 5.3. The superscripts make explicit the fact that the  $m_i$  are the magnitudes that are calculated after Equation 5.17 has been solved.

Transformation	LSF Error	$\sigma$
$m_y^{fit} = M_Y^{CAL} + 2.173 - 0.068(M_Y^{CAL} - M_H^{CAL})$	0.0068	0.0096
$m_i^{fit} = M_I^{CAL} - 17.03 + 14.08X + 0.388(M_R^{CAL} - M_I^{CAL})$	0.0724	0.0591
$m_g^{fit} = M_V^{CAL} - 10.57 + 8.025X + 0.502(M_B^{CAL} - M_V^{CAL})$	0.1261	0.1030

Table 5.5: Parameters from M13 exposures.

Filter	Airmass	Exp. Time	Cadence (s)	FWHM ( $''$ )	Avg. Background (counts/sec)	$\sigma$ Background (counts/sec)	Stars Found
<i>g</i>	1.003909	163.59	1-0-30-1	1.64	2.01	0.38	9104
<i>i</i>	1.011084	81.79	1-0-15-1	1.14	3.05	0.34	15,812
<i>y</i>	1.015034	163.59	1-0-30-1	1.32	1.80	0.28	2439

### 5.3.2 Crowded Field Photometry

We measured instrumental magnitudes of stars in M13: the Hercules cluster, a color image of which can be seen in Figure 1.1. We observed the cluster in a range of RA from 250.404-250.580 and DEC from 36.368-36.511 on two separate nights : 4/26/07 and 4/28/07. The raw data for M13 on 4/26/07 consists of 9 dithered up-the-ramp exposures for each of the *g*, *i*, and *y* filters, and is described in Table 5.5. Photometric analysis was performed on the slopefitted mosaics of M13 using the DAOPHOT algorithms DAOPHOT, GETPSF, SUBSTAR, NSTAR, and ALLSTAR in IRAF through the PyRAF interface. For details on parameters, refer to Appendix A.1, and for a description of DAOPHOT, refer to Davis [93]. The basic purpose of DAOPHOT is to identify point sources and measure the brightness of those sources alone. It does this by allowing the user to create a semi-analytic model that represents the point-spread function (PSF) of a star in the image and goes on to fit each star with that model. This technique is necessary for the case in which the field is “crowded”, i.e. the images of the stars are so close that they overlap and a pixel receives light from more than one source. The result of the DAOPHOT algorithms is an instrumental magnitude for each star.

In order to determine the zero-points of the instrumental magnitudes obtained with the DAOPHOT package, we obtained *g* and *i* magnitudes for the stars SDSS J16420106+362401.0 and SDSS J1646154.09+362348.8 from the Sloan Digital Sky Survey and compared them with ours. We find, roughly, that  $M_g^{CAL} = m_g^{H4RG} - 0.25$  and  $M_i^{CAL} = m_i^{H4RG} - 0.62$ . For *y*, we use the first equation in Table 5.4 and set the color term to zero since no stars could be found with *y* band magnitudes for reference in the field.

With the magnitudes adjusted for the zero point offset, color magnitude diagrams were created for the *g* – *i* filter pair and the *g* – *y* filter pair. These diagrams, shown in Figures 5.5 and 5.6, are qualitatively similar to those obtained from previous photometric studies for *B* and *V* filters. They show well the features of the red giant and blue straggler populations in the cluster. This is a good indication that the H4RG is capable of doing relative photometry between these bandpasses and verifies that the spectral responsivity is good out to the 1  $\mu\text{m}$  region. Similar results will hold for HyViSI detectors in general.

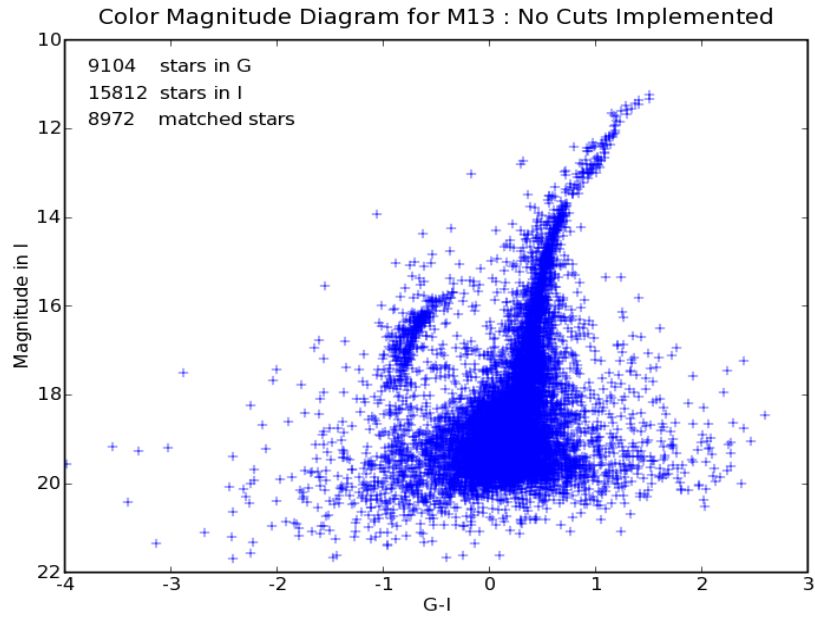


Figure 5.5: A Color Magnitude diagram for the M13 cluster in  $g$  and  $i$  bands.

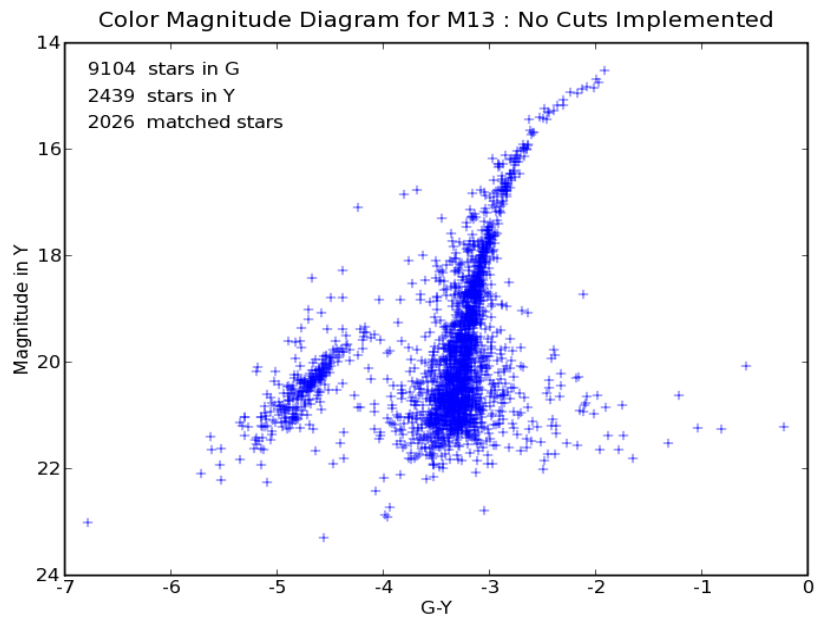


Figure 5.6: A Color Magnitude diagram for the M13 cluster in  $g$  and  $y$  bands.

### 5.3.3 High Speed Photometry with Guide Windows

Random, non-destructive access to pixels in a CMOS sensor open up intriguing possibilities for high speed astronomical photometry. The guide window capability of the HxRG allows one to skip around the detector and measure the flux of different stars without being forced to read pixels that are not in regions of interest. The time required to read out two separate windows will be independent of their separation in the sky, which is not a luxury of a CCD detector.

### 5.3.4 Variability Measurements of BE Lyn

As a preliminary test of photometry using multiple guide windows, the Delta Scuti star BE Lyn (HD 79889) was imaged with H2RG-32-147 over a period of several hours (see Section 5.2.7 for details). Delta Scuti stars are short period (0.05-0.25 days) variable stars that are believed to change brightness due to radial pulsation. BE Lyn is a particularly interesting example since its period has been measured numerous times and appears to be changing over time [94], [95], [96], [97], [98]. It has even been suggested that BE Lyn might possibly have a companion [99]. A brief timeline of the measurements and predictions surrounding the star is as follows:

**1987** Oja detects variability and reports a period of  $P = 0.0958697$  days for the oscillation in brightness [94].

**1991** Yanying et al. measure a change in the period relative to previous measurements. After using Observation vs. Calculation curves (O-C), they placed the average period at  $P = 0.095869547$  days and fit their data with an equation of the form [95]:

$$T_{max} = HDJ2446506.00774 + 0^d.095869547 \times E + 0.5 \times G \times E^2, \quad (5.19)$$

where  $T_{max}$  is the time of maximum,  $T_o = HDJ2446506.00774$  is an initial reference time,  $E$  is the cycle number, and  $G = -2.1 \times 10^{-12}$  days per cycle<sup>-2</sup> is the rate of period change. The value of  $G$  they reported (see Table 5.6) indicated the period was decreasing with time.

**1992** Qingquan et al. fit their own data and reported that the period is actually increasing with time [96].

**1994** Zhongli et al. place the average period at 0.09586963 days and concur the observations of Yang et al. that the period is increasing with time [97].

**1995** Kiss and Szatmary perform photoelectric photometry and fit the BE Lyn O-C curve supposing a cyclic period variation due to an orbital companion [99].

**2003** Derezas et al. make additional measurements and reject the presence of long-term light-curve shape changes. They place an upper limit on the rate of change of the period as

$\frac{1}{P} \frac{dP}{dt} = (-5 \pm 1.9) \times 10^{-8} \text{ year}^{-1}$  and admit no unambiguous conclusion can be drawn at that point in time [98].

Table 5.6: Variability Parameters for the Delta Scuti Star BE Lyn as measured by various authors. See references for additional measurements.

Author	Year Reported	$P$ (days)	$T_o$ (Julian Day)	G (days per cycle <sup>-2</sup> )
Oja [94]	1987	0.0958697	None	None
Yanying [95]	1991	0.095869547	HDJ2446506.00774	$-2.1 \times 10^{-11}$
Qingquan [96]	1992	0.09586938	HDJ2446506.0079	$1.1 \times 10^{-11}$
Zhongli [97]	1994	0.09586963	HDJ2449018.2684	$8.8 \times 10^{-12}$
Derekas [98]	2003	0.095869521	HDJ2449018.2681	None (See text above)

As this timeline indicates, the period of BE Lyn changes in a fashion that is not understood through conventional physical models. However, the period is extremely long in comparison to the sampling period attainable with the guide windows and provides a good target for testing the capability of the HyViSI to perform high speed photometry. An investigation was thus undertaken with H2RG-32-147 in order to examine the usefulness of reference correction with multiple guide windows and the stability of the photometric response over a long time span.

#### 5.3.4.1 Observations with Kitt Peak 2.1m and Reduction

Observations of BE Lyn were made through the  $i$  filter with H2RG-32-147 from 09:45 UTC until 13:00 UTC on the night of Dec 17, 2007. The staggered-reset-staggered-read-staggered-read (SRSRSR) multiple window mode was chosen (see Section 3.2.1) for these observations in order to allow alternation between the target star and a reference star whilst providing similar atmospheric noise for both integrations. The window size for both the target BE Lyn and the reference star GSC 03425-00544 was  $61 \times 61$  pixels, which yielded an integration time of roughly 0.08 seconds and a period of about 0.241 seconds ( $\sim 4$  Hz). Unfortunately, high cirrus clouds were present and the seeing was not nominal; it varied from 1.4-1.8 arcseconds over the night. Out of the approximately 100,000 windows collected (50,000 for each star), nearly 15,000 could not be used because of cloud cover or an extremely diffuse PSF.

After data collection, for each CDS window frame centroids were measured using the IDL FIND utility and then aperture photometry was performed with IDL APER. All relevant information was recorded to a MYSQL database for later analysis. To apply a correction with the reference star, the measured flux of the target was divided by the measured flux of the reference star on a point by point basis. After correction, a median filter was applied to the light curve of the target in order to remove outliers, reduce noise, and fill in the many missing data points.

### 5.3.4.2 Results

Figure 5.7 shows the instrument corrected magnitudes returned by APER for BE Lyn and the reference star during the 3 hour observation period. The variable nature of BE Lyn is unambiguously evident when compared to the reference star. The brightness of the reference star is relatively flat, but becomes broader near the end of the night and in areas where cloud cover obscured the field of view. Meanwhile, BE Lyn undergoes a  $\sim 0.25$  change in magnitude. The outlying points and gaps in the data for the reference star coincide with those of BE Lyn: a fact which is more easily observed in Figure 5.8, which shows the magnitude of BE Lyn after the flux has been normalized by the reference star. While the spread of data points grows greatly in the normalization (the read noise and shot noise are effectively multiplied in the division), the outliers are no longer evident, indicating the high magnitude outliers are caused by cloud cover or uniform atmospheric effects.

The missing data points and the fact that BE Lyn was only observed for 1.25 periods makes it difficult to precisely measure its period with this data set. Using an autocorrelation technique as well as a period searching program similar to the one described by Oja [94], our measurements place the period between and  $0.0958286 < P < 0.0961084$  days. A value in this range is consistent with previously measured periods. Previous O-C curves yield errors of  $10^{-3}$  days for predictions of the

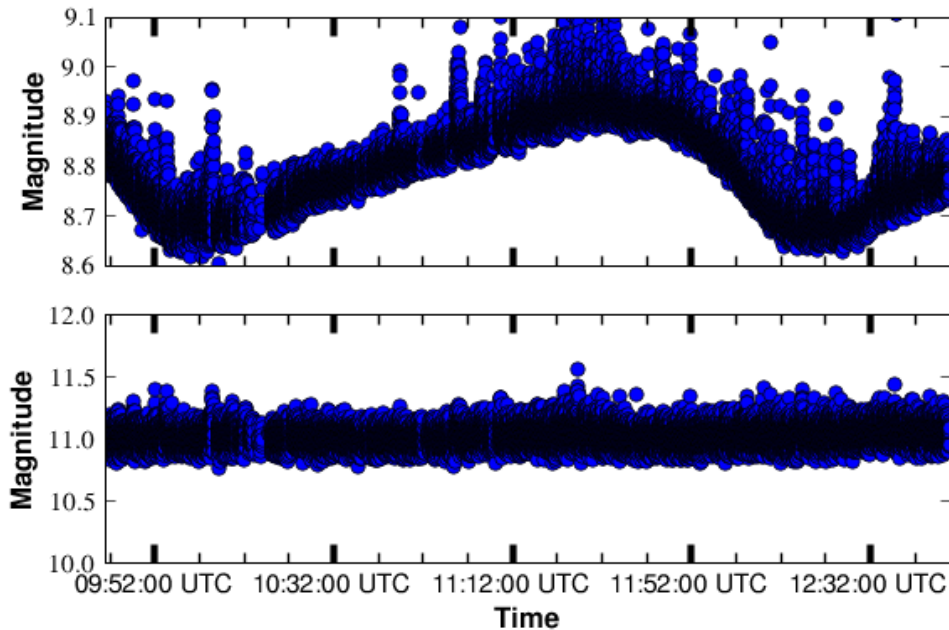


Figure 5.7: (Top) Magnitude vs. time plot for the Delta Scuti star BE Lyn over a 3 hour period. (Bottom) The same plot for the reference star GSC 03425-00544.

period, so the error in the present measurements are within reason.

The overall amplitude of oscillation in brightness for BE Lyn is measured to be about 0.21 magnitudes. No previous  $i$  band measurements could be found for this star, but the  $V$  band amplitude is reported as 0.39 magnitudes. The reference star fluctuations are 0.065 magnitudes RMS without any rejection of outliers. With the improved read noise obtained in recent laboratory measurements (20-30  $e^-$  read noise RMS was measured at the telescope; 8-10  $e^-$  in lab tests following the observations), the read noise contribution to the overall noise fluctuations in magnitude will be significantly diminished. Finger et al. have performed very similar measurements with a HgCdTe H2RG array on a magnitude 5 star and obtained an error of 0.026 magnitudes RMS with a read noise of 8.2  $e^-$  [100]. These results are very promising for high speed photometry with HyViSI sensors, placing them in good favor for observing fast variables like Delta Scuti stars, extra-solar planet transits and occultations, or other known or unknown “bumps in the night”.

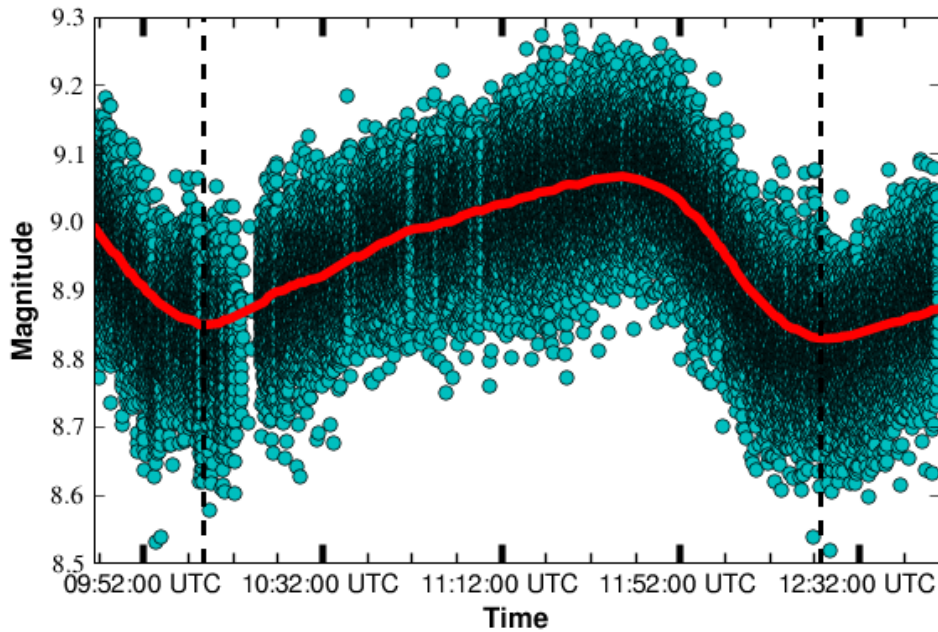


Figure 5.8: Magnitude vs. time plot for BE Lyn after normalization by the reference star. The cyan points show the raw data after normalization and the red line through them is a median filter that was applied to the data to reject outliers and interpolate the missing data points. The two dashed black vertical lines indicate the accepted period of oscillation, which is 0.0958697 days or 02:18:03 hours.

## 5.4 Astrometry

Astrometry is the precise measurement of positions and motions of celestial bodies. Because astronomical distances possess a large uncertainty, these measurements are usually confined to the two-dimensional projection of the sky as seen by observers on earth, and positions of astronomical objects are tabulated in catalogs as a set of two sky *angles* measured with respect to a set of reference points.<sup>3</sup> In modern astronomy, standard practice is to record coordinate information to the FITS image header at the time of observation using the world coordinate system (WCS), which greatly facilitates analysis of astrometric data and its transaction between astronomers [101]. With proper WCS information, positions in one image can be easily compared with those in another, regardless of the type of detector used or the epoch at which they were recorded.

As described by Monet, the apparent position of an object with respect to nearby reference stars is

$$Position = Constant + Proper\ Motion + Parallax + Perturbations \quad (5.20)$$

in each coordinate [102]. For one particular observation, the telescope, detector, and atmosphere must be considered as additional terms on the right hand side of this equation. As will be discussed, though, these terms can be removed with proper calibration techniques and using multiple exposures. Each term on the right side of Equation 5.20, aside from the constant one, is significant in astronomy and astrophysics. Measuring parallax is extremely important because it yields the most unambiguous distance measurements possible. In fact, all other distance estimates rely on parallax as the “bottom rung” of the cosmic distance ladder. Proper motion and perturbations of objects within our galaxy yield a great deal of information about the dynamics of the Milky Way as a whole in addition to smaller gravitationally bound systems such as binary stars. Also, extrasolar planets can be detected with precise, milli-arcsecond (mas) astrometric measurements. Astrometry is thus a very important facet of astronomy, and will become even more so as large scale surveys attempt to “map” the sky in finer detail.

While systematic errors in the relative positions of objects being measured by a given detector can be corrected for with proper calibration, *the accuracy* with which the detector can measure the individual positions is limited at a physical level. The pixel size (or more precisely, the plate scale in "/pixel), quantum yield, read noise, linearity, pixel and output crosstalk, and dark current all determine how well centroids can be measured on the array, and thus, what the astrometric error will be. Theoretical calculations and Monte Carlo simulations can be used to make predictions on the error, but in the end they must be compared to real data for validation.

In the following sections, the relative astrometric errors measured with HyViSI sensors at the

---

<sup>3</sup>The most common system is the *equatorial coordinate system*. Object positions are projected onto the *celestial sphere* and the angular coordinates of right ascension ( $\alpha$  or RA) and declination ( $\delta$  or DEC) serve as analogs to longitude and latitude, respectively. The zero position for RA is measured with respect to the First Point of Aries and the zero position for DEC is measured with respect to the celestial equator.

Kitt Peak 2.1m telescope are presented. The plate scale for the 18 micron pixel H1RG-022 and H2RG-32-147 detectors was  $0.227''/\text{pixel}$  and that for H4RG-10-007 was  $0.126''/\text{pixel}$ . In theory, the astrometric error measured with these detectors in terms of pixel units can be used to predict angular errors for other optical configurations.

### 5.4.1 Sources of Astrometric Error

There are a number of sources that contribute to astrometric error. The telescope optics and detector can cause distortions of the field in the final image. However, both of these are typically stable (although the distortion of the primary mirror may vary over its full range of motion) and can be corrected by applying a distortion map to the x-y pixel positions in the image. Atmospheric turbulence and read noise can lead to nonuniform, random errors in centroid positions across the focal plane. Both of these contribute greatly to error in a single, short exposure, but they can be diminished with long integration times or averaging multiple exposures. Finally, the optical system (e.g. the point spread function) and the aforementioned detector characteristics impose a base level error for the centroid positions in a given frame.

Following the methodology of Zacharias [103], the variance in a transformation of x,y centroid positions in a given frame into the average x,y positions in a reference coordinate map can be written as

$$\sigma_{astrm}^2 = \sigma_{atm}^2 + \sigma_b^2, \quad (5.21)$$

where  $\sigma_{atm}$  is the noise induced the atmosphere and  $\sigma_b$  is the base level noise level in an individual exposure. The factor of  $\sqrt{2}$  is removed because the transformation is done between an individual frame and a reference grid rather than two individual frames. It is important to note that this is for the shot-noise limited case. If faint stars are included and the detector is read-noise limited, an additional term  $\sim \sigma_{wn}/N_{reads}$  should be included, where  $\sigma_{wn}$  is the white noise and  $N_{reads}$  is the number of reads used to estimate the signal. With sufficiently bright stars, though, this term can be neglected. Since the dependence of  $\sigma_{atm}$  on integration time goes as  $t^{-1/2}$ , Equation 5.21 can be written as

$$\sigma_{astrm}^2 = \sigma_a^2 t^{-1} + \sigma_b^2, \quad (5.22)$$

where  $\sigma_a$  is the noise inherent in a semi-instantaneous realization of the atmosphere.

Equation 5.22 predicts that the astrometric noise will go down as  $t^{-1/2}$  and level out at  $\sigma_b$  for very long integration times. In this prediction, it is assumed that the telescope is being properly guided. For the case where the telescope is not being guided, an additional term  $\sigma_{tracking}$  must be added:

$$\sigma_{astrm}^2 = \sigma_a^2 t^{-1} + \sigma_b^2 + \sigma_{tracking}^2 \quad (5.23)$$

It will be shown that  $\sigma_{tracking}$  becomes significant for the unguided Kitt Peak observations after a

time of about 50 seconds.

### 5.4.2 Astrometric Reduction

Astrometric analysis of the Kitt Peak 2.1m data obtained with H1RG-022, H2RG-32-147, and H4RG-10-007 was conducted primarily with utilities in the IRAF IMCOORDS package. These utilities were accessed through the pyraf command language. The analysis carried out for a set of exposures (the final slopefitted images) on a given field consists of the following basic steps:

- 1) Use the WCSTools `scat` program to obtain coordinates, magnitudes, and proper motions for all stars in the field detected in the USNO CCD Astrograph Catalog (UCAC2) [104]. The UCAC2 catalog has a limiting magnitude of R=16 and a standard error of 70 mas.
- 2) Detect source positions in each exposure using the STARFIND utility in IRAF. STARFIND calculates centroids by convolving each source with a Gaussian of a specified FWHM, so the IMEXAMINE routine is used on each image to provide a good estimate of this. Center of mass centroids were also calculated for comparison, and found to produce very similar results.
- 3) Match x-y positions of stars in the image to RA/DEC entries in catalog using the IRAF utility CCXYMATCH. After matching the stars, a six parameter astrometric fit is performed. Two of the parameters account for rotation, two for scale, and two for linear shift. The fit yields an improved set of world coordinate system (WCS) coordinates for the image. With the new WCS, the x-y positions of each star are converted to RA and DEC, and these new celestial coordinates are written to a file.
- 4) After the RA and DEC values have been computed for all the images of the field, the average RA and DEC positions for each star are calculated. These average celestial coordinates constitute a *reference map* to measure the astrometric error. The reference map removes any systematic errors generated by the 70 mas error from the UCAC2 catalog and proper motions of the stars since the time at which they were observed.
- 5) Measure astrometric error for a given frame by comparing it to the reference map. The astrometric error,  $\sigma_{astrom}$ , is then given for each coordinate as:

$$\sigma_{astrom}^{DEC} = \sqrt{\sum_{i=0}^N (\delta_i - \delta_i^{Ref})^2 / N} \quad \sigma_{astrom}^{RA} = \sqrt{\sum_{i=0}^N (\alpha_i - \alpha_i^{Ref})^2 / N}, \quad (5.24)$$

where  $\delta_i$  and  $\alpha_i$  are the declination and right ascension of the  $i^{th}$  star in the individual frame, respectively,  $\delta_i^{Ref}$  and  $\alpha_i^{Ref}$  are the corresponding coordinates as measured in the reference map, and  $N$  is the total number of stars found in the frame.

The reduction was performed for a number of observed fields. In some fields, multiple exposure times were sampled; in others the same exposure time was used for a variety of pointings (as part of a dither sequence described in Section 5.2.6). The  $g,i,y$  filter set was used and the temperature of the detector did not leave the range of 170-180 K. The seeing conditions varied from 0.8-1.8 arcseconds, and an expected degradation of the astrometric accuracy is observed with the poor seeing conditions.

### 5.4.3 Astrometric Results with H2RG-32-147 and H1RG-022

As was discussed in Section 5.2.7, most of the Kitt Peak observations were done without telescope guiding. For short exposure times, the tracking induced errors are expected to be negligible in comparison to the read noise and atmospheric errors. For long exposures, the read noise and atmosphere should average out, but the tracking errors are expected to produce significant error in the right ascension because of the oscillations described. This is precisely what is seen in Figure 5.9. The RA and DEC errors both go down approximately as  $t^{-1/2}$  for exposure times of less than 50 seconds and reach a minimum around 7-9 mas, but then begin to rise thereafter. The rise is worse for the RA because of the large amplitude oscillations of the telescope pointing along this axis.

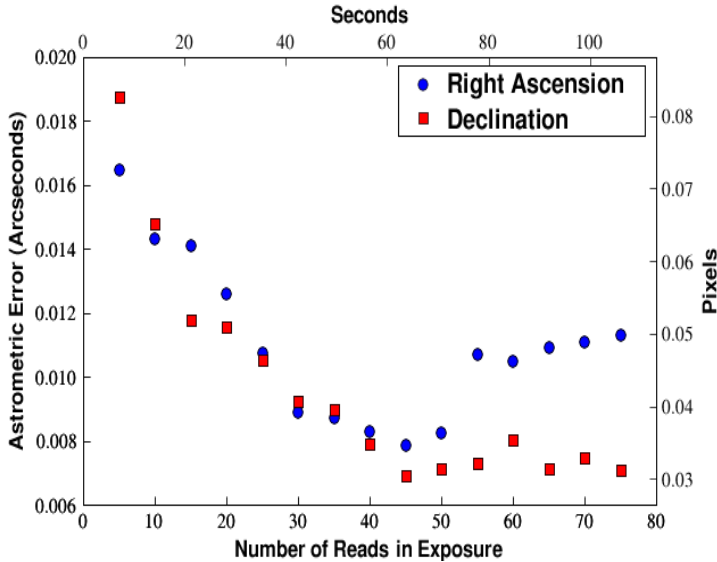


Figure 5.9: Astrometric error vs. exposure time for the open cluster NGC 956 observed with H2RG-32-147 in UTR mode. Each data point represents the average RMS deviations of 15-70 measured centroid positions (depending on filter and exposure time) from the reference map positions for a given exposure time. The average is taken across images from exposures in  $g,i,y$ . The large error in RA at long exposure times is due to the unguided operation of the telescope.

The situation improves in the case where H2RG-32-147 was simultaneously taking long exposures and guiding the telescope (details are explained in Section 3.3). For these exposures, the oscillations in RA are greatly reduced and the drift in DEC is not detectable. Table 5.7 shows a comparison for two 180 second exposures, one taken with H1RG-022 with no guiding and one taken with H2RG-32-147 with guiding. The astrometric error in DEC is comparable for both cases: about 6.5 mas. The error in the RA is larger without guiding, but achieves a similar value to the DEC value when the telescope was guided.

Table 5.7: Comparison of the measured astrometric error for two 180 second exposures. NGC 2419 was observed with H1RG-022 while the telescope was not being guided and SA0 116737 was observed with H2RG-32-147, which simultaneously guided the telescope in guide mode. The exposure time,  $t_{exp}$ , is listed along with the error in RA and DEC in units of pixels (pix) and milliarcseconds (mas). Both detectors have 18 micron pixels and the plate scale is  $0.227''/\text{pixel}$ .

Field	RA	DEC	$t_{exp}$ (s)	$\sigma_{RA}$ (mas)	$\sigma_{RA}$ (pix)	$\sigma_{DEC}$ (mas)	$\sigma_{DEC}$ (pix)	Guided
NGC 2419	$07^h 38^m 08.51^s$	$38^\circ 52' 54.9''$	204.0	9.02	0.040	6.75	0.030	No
SA0 116737	$08^h 25^m 01.06^s$	$09^\circ 25' 33.8''$	196.8	6.30	0.028	6.23	0.027	Yes

From these results, it can be concluded that the base level astrometric error for the configurations with H1RG-022 and H2RG-32-147 mounted to the Kitt Peak telescope ( $0.227''/\text{pixel}$ ) is about 6.3 mas. This amounts to 0.028 pixels (slightly greater than  $1/40^{th}$  of a pixel). The 0.028 pixel accuracy can, in principle, be used to predict the astrometric accuracy for a different optical system.

#### 5.4.4 Astrometric Results with H4RG-10-007

Results obtained with H4RG-10-007 showed very poor astrometric accuracy. This is primarily because the large tracking errors were not known at the time and the shortest exposure time used on a field suitable for astrometry was 81 seconds. As shown in the previous section, tracking errors are clearly a problem for exposure times of this length. Other factors include a large CDS read noise of 25-30  $e^-$ , electrical pickup from the readout electronics, and a large signal reset anomaly brought about because of a  $V_{RESET}$  value of 90 mV.

The best results with this device were about 9 mas in both RA and DEC for observations of M13. Since the pixel pitch is 10  $\mu\text{m}$  pixels for this device and the plate scale was  $0.126''/\text{pixel}$ , this translates to about 0.07 pixels. With an identical H4RG model, Dorland et al. measured accuracy of  $1/30^{th}$  of a pixel at 180 seconds exposure time and predict  $1/40^{th}$  of a pixel for longer, guided exposures [40]. With proper guiding, biasing, and read noise reduction to a level of  $10e^-$ , the astrometric error for H4RG-10-007 is expected to improve to this level.

## 5.5 Telescope Guiding in Guide Mode

Modern telescopes use very precise mechanical motors to track celestial objects across the sky while their location changes due to the rotation of the Earth.<sup>4</sup> The job is slightly easier for equatorial-mount telescopes that only need to adjust in right ascension (RA) than it is for altitude-azimuth telescopes that must adjust in right ascension *and* declination (DEC) to compensate for the sidereal motion of the heavens. However, even for equatorial-mount telescopes with the most sophisticated motors available it is an imperfect process. The majority of telescopes must keep their pointing accurate to less than an arcsecond in order to prevent “smearing” of stars and galaxies while they are being imaged.

The widespread solution in astronomy is to use a “guide star” to correct for any errors in the telescope tracking, the idea being that if the sidereal motion is being properly accounted for, a given star should stay in the same physical location  $(x_o, y_o)$  on the focal plane of the telescope. If any movement in the location  $(\Delta x, \Delta y)$  is detected (by a CCD or other imaging detector), tip/tilt corrections are made in the pointing of the telescope in order to bring the star back to its original location and make  $\Delta x = \Delta y = 0$ . Usually a sufficiently bright guide star is used to track offsets while a very dim object is being imaged in a long exposure.

If a CCD is being used as a “science sensor” to make the long duration exposure, it cannot be simultaneously used to guide. Accessing the pixels that contain the guide star would result in a destructive read of the entire array (the charge is shifted out of the pixels). Thus, a separate “guide sensor” is required to measure  $\Delta x$  and  $\Delta y$ . In contrast, because of the non-destructive readout and random access capabilities inherent in CMOS detector architecture, a CMOS device can act as both the guide and science sensor simultaneously. In particular, the Teledyne HxRG multiplexer has been designed with a special “guide mode” to accomplish this [22, 100]. Such capability is of great advantage for large focal plane arrays that consist of many detectors since any one of them can be used to track a guide star while it simultaneously participates in the science exposure.

Another benefit of the guide mode operation is that saturated pixels can be reset while the rest of the array integrates light. Resetting the saturated pixels prevents the dark current from hot pixels and photocharges generated by bright stars from blooming into neighboring pixels and eliminates output crosstalk. This is very advantageous for long exposures in which both bright stars and very dim objects are present.

### 5.5.1 Purpose of Experiment

Laboratory measurements and calculations can provide some indication of the impact that interpixel capacitance (IPC), read noise, nonlinearity, and image persistence will have on the ability of a HyViSI detector to guide a telescope. For instance, convolving the pixel impulse response with a

---

<sup>4</sup>This motion is referred to as *sidereal motion*.

simulation of the telescope point spread function and folding in read and shot noise will provide an estimate of the expected signal to noise and centroid accuracy for a stable point source. However, it is not immediately clear what subtle effects atmospheric turbulence and scintillation will induce when latent images are present (see Section 7.2). For instance, if atmospheric effects displace the stellar image by a few pixels for several seconds, the latent image that forms might cause errant centroid values for subsequent measurements after the star has returned to its original location on the detector. Reproducing such effects would require very elaborate simulations or a complicated laboratory setup. And in fact, analytical models and simulations used to fit latent images based upon the flux and fluence of the offending image result in large errors (see Section 7.5.2), so this might not be a valid option to pursue.

To directly measure the impact of these second order effects and see whether or not the HyViSI can accurately track a star, we used H2RG-32-147 to guide the Kitt Peak 2.1m telescope. Operating in guide mode, it was able to simultaneously obtain high dynamic range exposures of the full field and track a guide star over long periods of time. For a description of the experimental setup used for guiding, the reader is referred to Section 5.2.8.2. In the following sections, we show measurements made from long exposures with and without guiding and discuss the results.

### 5.5.2 Results without Guide Mode

To attach the RIDL dewar to the Kitt Peak 2.1m telescope, it was necessary to remove the CCD guider from the instrument rack. As a consequence, the default configuration for our observing runs had the TCS tracking the sky at the sidereal rate with no guiding offsets being issued to account for errors in tracking.

Recognizing that tracking errors would be an issue, the typical cadence we used for our science exposures was a set of 9 or more dithers with short ( $< 1$  minute) exposures in each filter. The tracking errors during these short exposures are very minute, so they do not smear the image, and we only issued offsets between exposures. In software we account for both the controlled dither offsets of the telescope and any errors in the pointing by aligning the dithered images with bright stars.

However, in some cases we took long exposures without any guiding. The slopefit from such an exposure, taken in  $i$  band, is shown on the left in Figure 5.10. No dark subtraction or flat field has been applied so hot pixels, defects, and non-uniformity are present in the image. As exemplified by this figure, tracking errors clearly show up in long exposures taken with H1RG-022 and H2RG-32-147. Because the telescope leads or lags the sidereal motion, the light from the stars is smeared out over the pixels so that they have a “jelly-bean” like appearance. We will provide a quantitative description of this in Section 5.5.4.

The bright star in this exposure is SAO 54817, a star with magnitude 6.55 in the V-band and 4.717 in the J-band. The flux falling on the detector was thus somewhere between 400-900 mW/m<sup>2</sup>

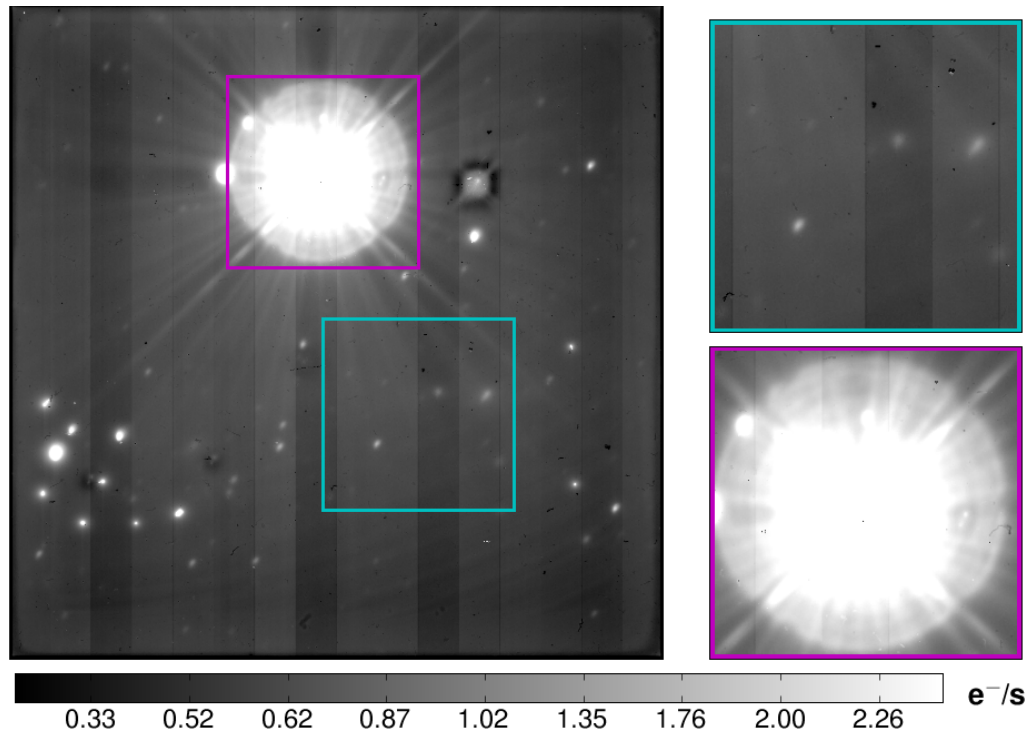


Figure 5.10: (Left) Full frame slopefit to a 1770 s exposure taken with H1RG-022 with no guiding. (Right) A zoomed view of the box enclosing the very saturated star SAO 54817 is shown at bottom right. The light from this star has consumed a circular region of pixels with a radius of 50 pixels. The box at upper right shows an area away from the guide window that contains three stars of irregular shape. Both boxes are  $300 \times 300$  pixels.

in  $i$  band. By the end of the exposure, the light from this star has saturated a circular region out to a radius of 50 pixels. For the dimmer stars, image blur due to the tracking error is clearly evident, as evidenced in the top right image of Figure 5.10.

### 5.5.3 Results with Guide Mode

An example guide exposure is shown in Figure 5.11. It is a slopefit (no dark subtracted or flat field to remove hot pixels and defects) to a 2597 s  $i$  band exposure of an  $8' \times 8'$  field centered around the star IRAS 09595+2513, which was used as the guide star. The magnitude in V of this star was not found in any catalogs, but is listed as 5.807 in J and 4.594 in K. It has colors of a late M star, so  $V-K \sim 6.2$ , and thus  $V \sim 10.8$  [105]. Based upon these colors, in  $i$  band we expect a flux of 20-170  $mW/m^2$  was falling on the detector.

For this exposure, 220 reads of the full frame were recorded and in between them 200 CDS frames of the window were read out. The window was  $35 \times 37$  pixels and the time for a CDS pair was

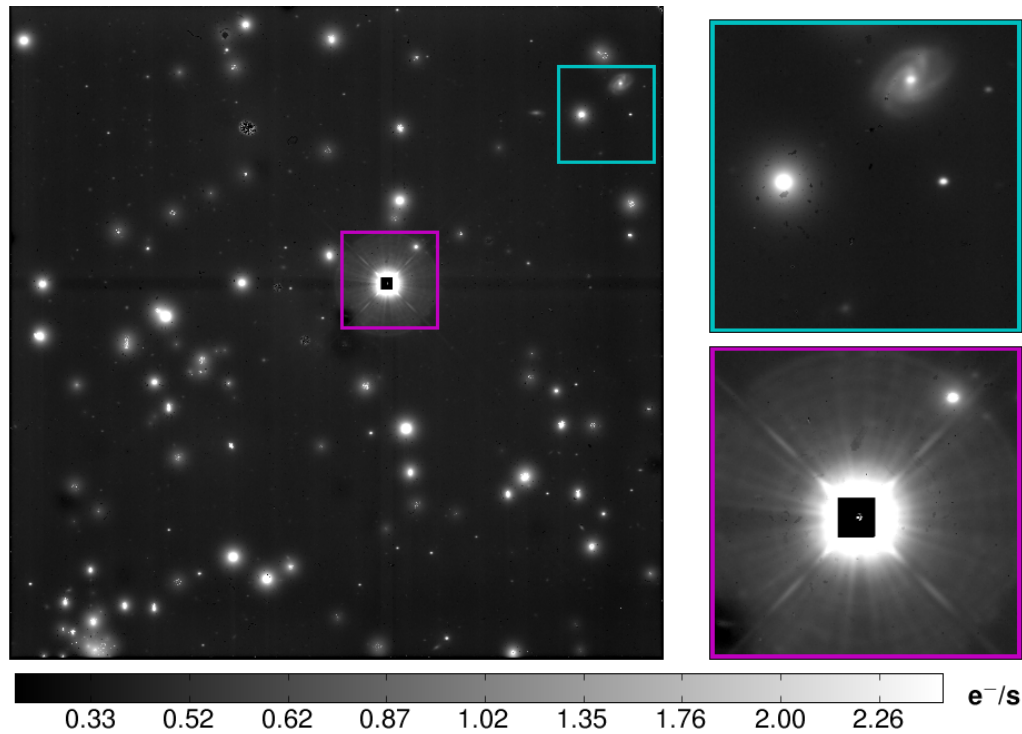


Figure 5.11: (Left) Full frame slopefit to a 2597 s exposure taken with H2RG-32-147 while it was operating in guide mode to guide the telescope. No flat field or dark subtraction was applied. (Right) The box blown up at the bottom right shows the guide window that has been reset constantly during the long exposure at the center of the bright star IRAS 09595+2513. The box at upper right shows an area away from the guide window that contains two faint galaxies. Both boxes are  $300 \times 300$  pixels.

$t_{sw} = 40.9$  ms, which corresponds to approximately 25 Hz sampling. Using the flux estimate above, at this sampling rate the maximum fluence was 0.8-6.8 mJ/m<sup>2</sup>. All of the 200 frames were coadded and the centroid of the star was calculated from the final sum using a  $9 \times 9$  box at the middle of the full window, which yielded an effective guiding rate of 0.12 Hz. This is slow in comparison to typical guiding rates; atmospheric disturbances average out on the order of seconds and any centroid displacement after that length of time is attributed to tracking error. However, we did not issue offsets faster than this because offsets less than  $0.3''$  were found to be inaccurate, resulting in increased blurring of the image (see Section 5.2.8.2).

#### 5.5.4 Comparison between Exposures with and without Guide Mode

Figure 5.12 shows a close up-image of a star taken from each of the long exposures described in the previous sections along with a quantitative comparison of the stars in terms of their ellipticity and

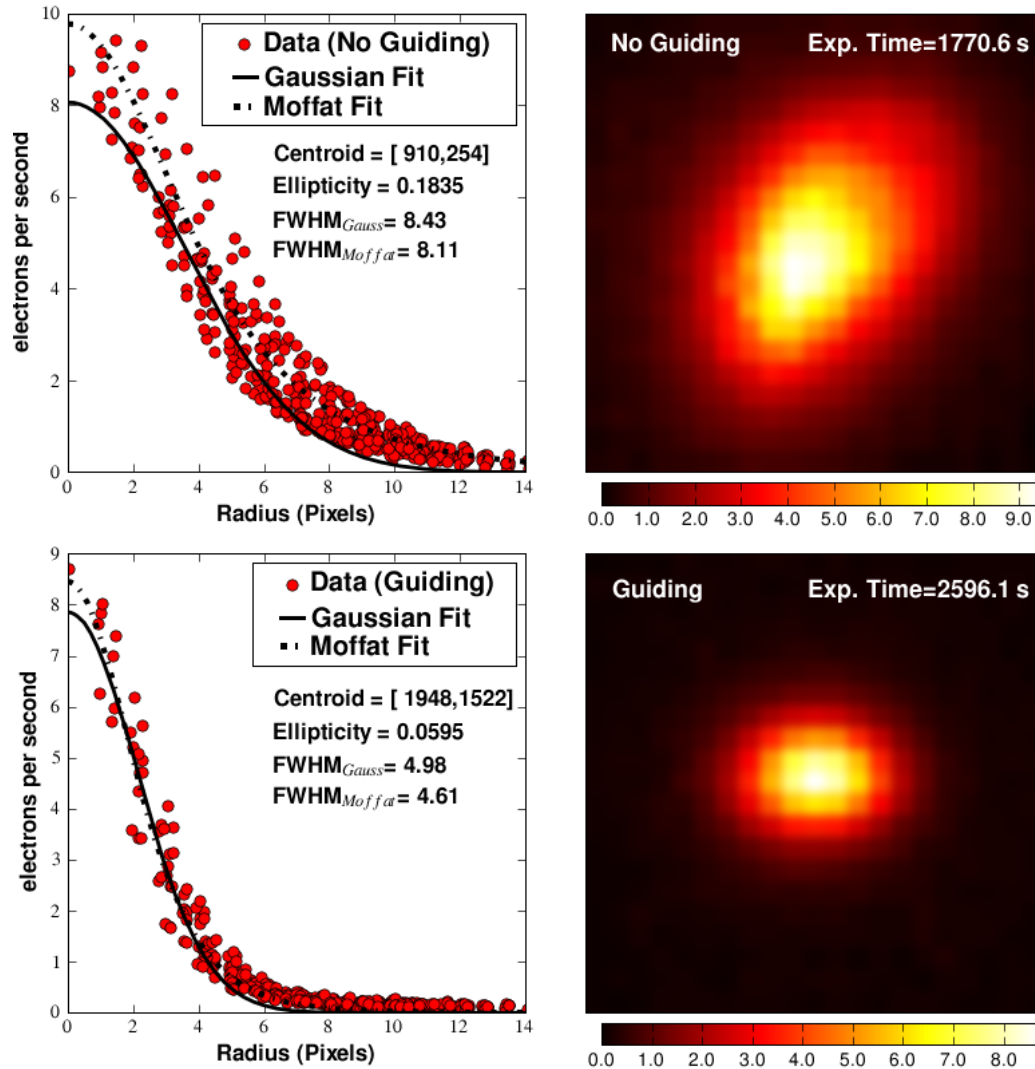


Figure 5.12: The top two figures show a stellar profile from a 1770 s exposure taken with H1RG-022 without telescope guiding. The bottom two show the radial profiles from a 2597 s exposure taken with H2RG-32-147 while it was being used in guide mode to provide offsets to the telescope.

FWHM. We consider these here along with the difference in limiting magnitude in each exposure and the saturation of pixels surrounding the central star.

**Ellipticity** The stars in the guide mode slopefit do have a slight average ellipticity of 0.06 along the x direction. We note that this is the direction that coincides with right ascension: the direction that was corrected more frequently. However, the ellipticity is 3 times smaller than it was

when the telescope was not being guided. In the latter case the ellipticity of the stars was clearly induced by tracking errors, particularly the oscillations discussed in Section 5.2.8. It is clear that the guiding succeeded in diminishing the ellipticity of the stars.

**Full Width at Half Maximum** As shown in Figure 5.12, the FWHM is significantly smaller when the telescope was guided. It is just slightly larger than the seeing of  $1.0''$  (4.3 pixels) recorded for the night. The seeing on the night when we imaged SA0 54817 was actually slightly better at approximately  $0.9''$ . We thus conclude that the smaller image blur is a result of guiding rather than atmospheric conditions.

**Limiting Magnitude** In terms of faint sources, in the guide mode slopefit we are able to detect galaxies and point sources in the Sloan Digital Sky Survey catalog down to a magnitude of 23.1 in the i-band at the  $3\sigma$  level. This is much fainter than the limiting magnitude in i-band of approximately 21.5 that we obtained by matching sources in the USNOA-2.0 catalog with those in our exposure with no guiding.

There is, however, a discrepancy in exposure times. To properly account for this difference, we can extrapolate for the limiting magnitude with no guiding based on theory using a standard equation for signal to noise prediction (see Appendix B). The background sky fluxes  $B$  and dark current  $D$  in the exposures are very similar; the real difference is the radius subtended by the faint stars in the exposures,  $r_{source}$ . Figure 5.13 shows the expected limiting magnitude at a certain exposure time for the guiding case where  $r_{source} \sim 7.2$  pixels and  $B \sim 6.8 e^-/s$ , as well as the non-guiding case where  $r_{source} \sim 17$  pixels and  $B \sim 10.6 e^-/s$ .

The behavior is easy to understand intuitively. When the telescope is not tracking a star properly, its light gets distributed into a large area of pixels rather than being concentrated in a small region. The light from the star then tends to blend in with the background sky light and be confused with

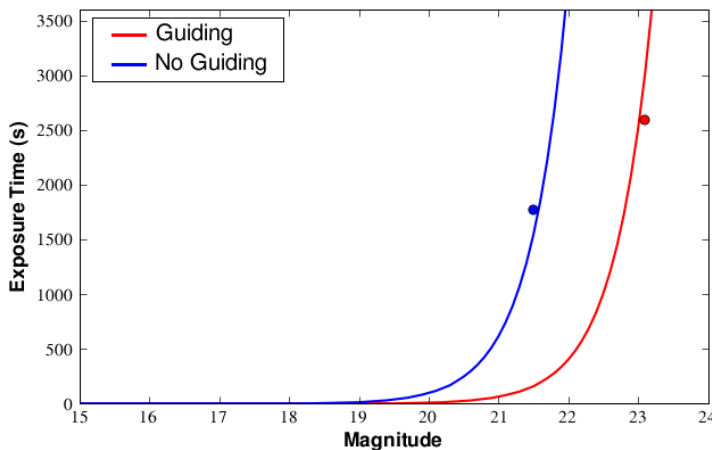


Figure 5.13: Theoretical exposure time required to reach limiting magnitude with a signal to noise ratio of 3 for the cases where the telescope is being guided by H2RG-32-147 (right curve) and where it is simply trying to track stars at the side-real rate with H1RG-022 (left curve). The data points are also plotted as circles. The difference is due almost entirely to the disparity in PSFs.

dark current, especially near the edge of the star. Taking into account the disparity in  $r_{source}$ , we see in Figure 5.13 that for an hour long exposure the guide mode will go about 1.4 magnitudes fainter.

### 5.5.5 Saturated Pixels

When we implemented guide mode with H2RG-32-147, resetting the pixels in the guide window did not prevent the surrounding pixels from reaching saturation. However, the reason that the surrounding pixels saturated was not because the accumulated charge from the bright star bloomed into its neighbors. Rather, the diffraction of light from IRAS 09595+2513 into the pixels immediately surrounding the guide window is significant enough to generate  $\sim 50 e^-/s$  and fill the pixel wells after about 1500 seconds. Further out, the rate of carrier generation is smaller, but still enough to saturate the pixels in 2500 seconds.

We note that the operation of guide mode will indeed prevent charge blooming if the guide window is large enough to contain all of the pixels integrating photocharge from the star. We have also used it successfully in resetting a hot pixel so that it does not spill into its neighbors. One additional benefit is that resetting the brightest portion of the stellar image prevents crosstalk between detector outputs. For  $N_{out}$  detector outputs and  $N_{pix/row}$  pixels per row, this effect manifests itself as  $N_{out}$  repeated images of the star evenly spaced across the columns at intervals of  $N_{pix/row}/N_{out}$  pixels (for certain read directions). More details can be found in Finger et al. [100] and in Section 6.2.2.

### 5.5.6 Summary of Results

The results from the long exposures with and without the implementation of guide mode are shown in Table 5.8. As is expected for a guided camera system, the ellipticity and FWHM are reduced and the limiting magnitude is boosted when we use H2RG-32-147 to guide the Kitt Peak 2.1m telescope.

Table 5.8: Quantitative comparison of long exposures obtained when the telescope was being guided by H2RG-32-147 and simply tracking at the sidereal rate.

Parameter	H1RG-022: No Guiding	H2RG-32-147: Guide Mode
Ellipticity ( $\ \vec{e}\ $ )	0.18	0.06
FWHM <sub>Gauss</sub> (pixels)/(")	8.70 (2.02)	5.90 (1.37)
FWHM <sub>Moffat</sub> (pixels)/(")	7.24 (1.67)	4.60 (1.07)
Atmospheric Seeing (pixels)/(")	3.9 (0.90)	4.31 (1.00)
$M_{Lim}$ in 3600s exposure	21.9	23.3

### 5.5.7 Discussion

The ellipticity and FWHM of the stars in both guided and unguided mode agree very well with the values predicted using Equation 5.13 along with the nightly seeing conditions and average drift rates for  $m_{DEC}$  and  $m_{RA}$ . The measurements indicate that image persistence brought about by high flux/low fluence integrations of the guide star in window mode and pixel nonlinearity do not produce significant errors in the centroid accuracy. Based upon the brightest star used to guide, SAO 81129 ( $J \sim 3.98$ ) observed in  $y$  band, this is true for fluxes  $< 2 \text{ W/m}^2$  and fluences  $< 80 \text{ mJ/m}^2$ . For future star tracking applications, it should be sufficient to consider the standard parameters of read noise, dark current shot noise, interpixel capacitance, etc. when predicting performance, at least for fluxes and fluences below these limits. It is expected that brighter stars and longer integration times can still be used, but to address the situation concretely, additional measurements need to be carried out. In the meantime, simulations are being attempted to address the issue (see Section 7.5.2.1).

Although it was not discussed in the previous sections, one very important aspect of using the HxRCs in guide mode is the behavior of the outermost rows and columns in the guide window. Regardless of the state of the pixels outside the window, the first column in the window will generally have a slightly higher signal due to settling effects after switching rows in the clocking sequence. This offset should subtract out in a CDS, but the column will suffer from increased noise in the CDS. There is also a large dependence of the outer rows and columns on the state of the pixels outside the window due to IPC, as shown in Figure 5.14. If the rows and columns immediately outside of the window have a large voltage, they will pull the outer rows and columns of the window up in signal. The coupling manifests itself as both an offset and, in cases where the signal is sufficiently high, an increased apparent photocurrent for the outer rows and columns of the window. An easy way to deal with this problem is to make the guide window slightly larger than the region that will be used for the centroid calculation so that the outer rows and columns can be ignored.

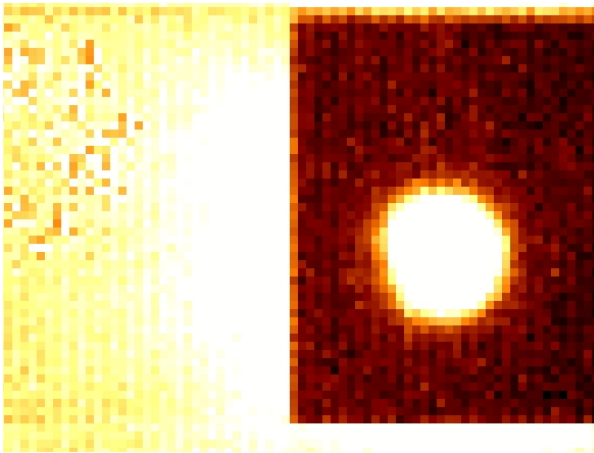


Figure 5.14: An image taken from a full frame read of the detector while it was operating in guide mode. When the pixels inside the guide window (dark pixels) are continuously reset while the pixels outside integrate a large photocurrent (bright pixels), the outer rows and columns of the guide window see an increased signal due to IPC. Making the window larger than the light envelope of the star prevents the outer columns and rows from contaminating the centroid calculation.

## 5.6 Near Infrared Response

Conventional back thinned CCD detectors in astronomy have a weak red response and virtually no response at wavelengths above 800 nanometers. Since the interaction depth of near infrared photons is about 25 nm at 750nm (and grows rapidly with increasing wavelength), thinned CCDs simply lack the thickness to absorb them efficiently. As such, the Near-Infrared (NIR) regime above 750 nm has been the territory of non-silicon based hybrid CMOS infrared detectors.<sup>5</sup> From a practical standpoint, camera systems using these detectors are more involved since they require temperatures below 80 K (20-80 K for HgCdTe and 30 K for InSb [18]). HyViSI detectors extend into the NIR without requiring such heavy cooling.

The  $y$  filter provides a perfect opportunity to test the HyViSIs in between the traditionally classified “optical” and “infrared” bands [92], and the Orion Nebula provides a perfect target since it emits strongly in both bands. The image shown in Figure 5.15 is a three color RGB mosaic of the heart of the Orion Nebula (M42) taken with H1RG-022 through the  $g$  (blue),  $i$  (green), and  $y$  (red) filter set. It was the product of combining the slopefits from 45 dithered exposures in each filter. Each exposure in  $g$  and  $i$  was 5.1 seconds long (15 reads UTR) and the ones in  $y$  were 10.2 seconds (30 reads UTR). The scales used in combining the final mosaics in each filter were set to match the quantum efficiencies measured by Dorn et al. [49] – 0.82 ( $g$ ): 1.00 ( $i$ ): 0.15 ( $y$ ). In other words, 10  $e^-/s$  in the  $i$  band has the same bitmap value as 1.5  $e^-/s$  in  $y$  and 8.2  $e^-/s$  in  $g$ .

The purpose of presenting this image is not to introduce new quantitative or scientific analysis of this region. The Orion Nebula has been studied extensively in all wavelengths, particularly the visible and infrared [41]. Rather, the goal is to verify that the quantum efficiencies reported from HyViSI laboratory measurements – remembering that techniques like photon transfer have resulted in QE > 100% in some cases – are accurate. Qualitatively, the results are exactly what is expected from measurements made in previous infrared and visible studies: the bright O and B stars of the Trapezium cluster show up prominently in all three filters, the HII region glows strongly in  $g$  and  $i$  and hardly at all in  $y$ , and the stars obscured by dust and gas hardly show any signal in  $g$  but glow strongly in the near infrared  $y$  band. This provides confirmation that the quantum efficiencies measured in the laboratory are valid and the HyViSI performs as expected at 1 micron. Again, the uniqueness of this is that optical and near infrared observations were made with the same silicon based detector operating at 160K.

The bright horizontal banding and ghost images that appear on every output in the rows with a very bright star are artifacts of the detector and ARC electronics. Since the H1RG was operated in 16 output mode, there are 15 ghost stars for each bright star in an individual exposure. The mosaic processing helps to reduce their amplitude and blend them together. The ghosts and banding are examples of output crosstalk, which will be considered in depth in the next chapter.

---

<sup>5</sup>There seems to be some disagreement between the exact definition of the various infrared bands in the literature. For the purpose of this study, the NIR band will be considered to be 750-1400 nm.

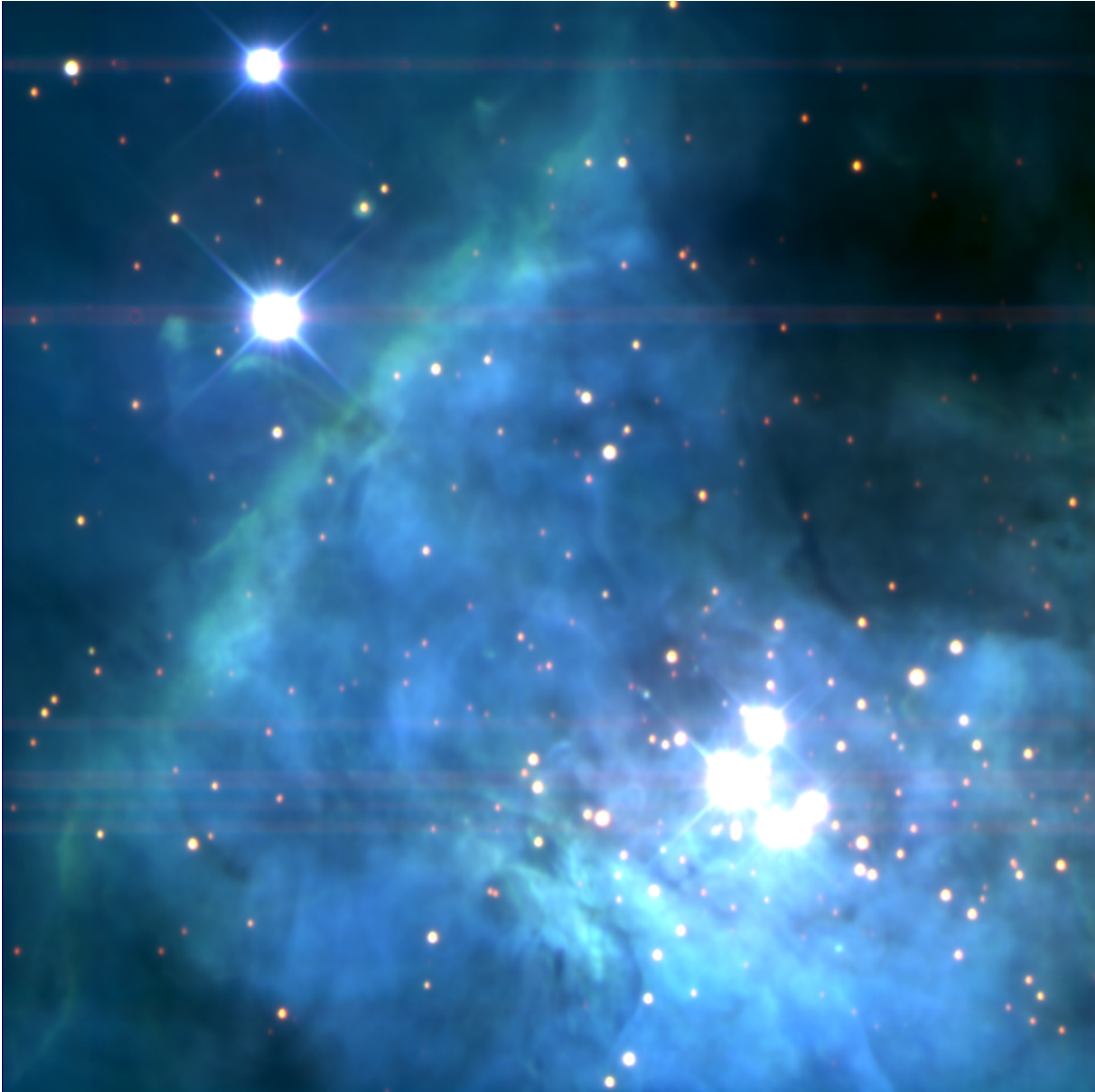


Figure 5.15: Tri-color image of the Orion Nebula (M42) taken in *g*, *i*, and *y* filters. The *y* band is shown in red, *g* in blue, and *i* in green. Other exposure details are listed in the text. The vast majority of stars are not visible in *g* and *i* because of obscuring gas and dust, but show up in *y* because the infrared wavelengths penetrate the dust.